CHALMERS
UNIVERSITY OF TECHNOLOGY

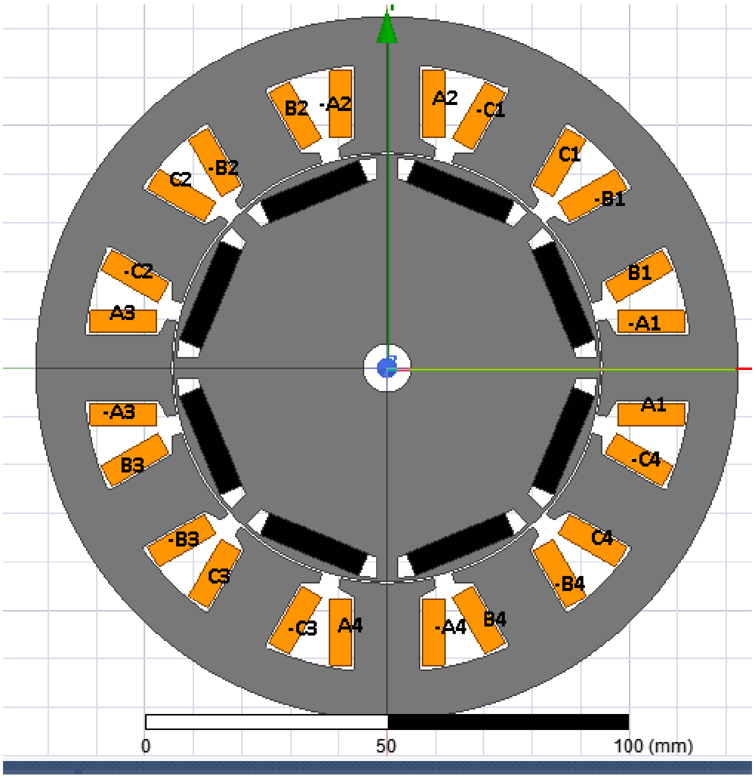
B2
-A2
A2
-C1
C2
-B2
C1
-B1
-C2
A3
B1
-A1
-A3
B3
A1
-C4
-B3
C3
C4
-B4
-C3
A4
-A4
B4
0
50
100 (mm)

Modelling and control of a dual three-phase PMSM

With focus on performance at various failure modes

Electric Power Engineering, MSc

DAVID AHLBÄCK
RAFAEL BAUSONE

DEPARTMENT OF ELECTRICAL ENGINEERING

CHALMERS UNIVERSITY OF TECHNOLOGY
Gothenburg, Sweden 2021
www.chalmers.se

Master's thesis 2021

Modelling and control of a dual three-phase PMSM

With a focus on performance at various failure modes

DAVID AHLBÄCK
RAFAEL BAUSONE

Department of Electrical Engineering
Division of Electric Power Engineering
Chalmers University of Technology
Gothenburg, Sweden 2021

Modelling and control of a dual three-phase PMSM
With focus on performance at various failure modes
DAVID AHLBÄCK
RAFAEL BAUSONE

© DAVID AHLBÄCK, 2021.
© RAFAEL BAUSONE, 2021.

Supervisor: Johan Åström, Aros Electronics
Examiner: Torbjörn Thiringer, Department of Electrical Engineering

Master's Thesis 2021
Department Electrical Engineering
Division of Electric Power Engineering
Chalmers University of Technology
SE-412 96 Gothenburg
Telephone +46 31 772 1000

Cover: Cross-section of the prototype machine showing the winding arrangement.

Typeset in LaTeX
Printed by Chalmers Reproservice
Gothenburg, Sweden 2021

Modelling and control of a dual three-phase PMSM
With focus on performance at various failure modes
DAVID AHLBÄCK
RAFAEL BAUSONE
Department of Electrical Engineering
Chalmers University of Technology

Abstract

This thesis analyses the performance and different control methods of a dual-winding PMSM under various fault-scenarios. The machine investigated has a segregated dual-winding layout with no neutral connections. A physical-phase variable model is implemented utilising FEM-data in order to model the non-ideal properties of the system and to implement faults. Simulations are compared against experimental results on a prototype machine with satisfactory results.

The focus is on the torque capability and torque ripple, where healthy dual operation results are compared against three-phase open and one-phase open scenarios. Three different post-fault control approaches are investigated. Analytical calculations are performed for short-circuit faults and the harmonic contents of the different open-phase scenarios are analysed. The main approach is to investigate control methods where no additional hardware is required.

It is found that one winding can comfortably carry half the rated load if the other is disconnected. The open-phase scenarios are mainly analysed for one winding at the time where two different post-fault control methods are applied. The so-called pre-fire and per-phase methods. Both prove to output higher torque in post-fault operation than if no action is taken. A resonance controller method is also investigated, which proves to reduce harmonic content and torque ripple for all operating scenarios. However, it does not function satisfactorily as the sole open-phase post-fault controller with the winding arrangement used. The analytical calculations indicate a very low tolerance for short-circuit faults.

At low torque loads the machine is found to function remarkably well during single phase-open operation. Post-fault control algorithms are however essential if a higher torque output is required.

Keywords: PMSM, fault-tolerant, Physical phase-variable modelling, dual-winding, FEM.

Acknowledgements

First of all, we would like to thank Aros Electronics and CTO Magnus Wide for giving us the opportunity and taking us in as thesis workers. We want to thank our main supervisor at Aros, Johan Åström, for all the time spent giving us great inputs and guidance long the way. A huge thank you goes out to Spyros Gryparis, for all the work making it possible for us to perform the lab tests, as well as for taking time out of his busy days for fruitful discussions. We also want to thank Daniel Chädström at Aros for providing us with the per-phase controller and the idea of implementing it.

Finally, we would like to thank Torbjörn Thiringer for taking us on as thesis students and for the swift and constructive feedback throughout the project.

David Ahlbäck, Rafael Bausone, Gothenburg, May 2021

Contents

1 Introduction **1**
1.1 Aim . . . 2
1.2 Scope . . . 2

2 Theory **5**
2.1 PMSM machine design . . . 5
2.1.1 Windings . . . 6
2.2 Modelling of PMSM machine . . . 8
2.3 Inverter theory . . . 9
2.4 DQ-transformation . . . 11
2.4.1 Harmonics . . . 12
2.5 Control theory . . . 13
2.5.1 IMC controller design . . . 14

3 Fault tolerant drive systems **17**
3.1 Possible faults . . . 18
3.1.1 Winding short-circuit Faults . . . 18
3.1.2 Open phase faults . . . 19
3.2 Fault mitigation approaches . . . 21
3.2.1 Fault tolerant machines . . . 21
3.2.2 Fault tolerant Inverters . . . 21
3.2.3 Post-fault control methods . . . 23

4 Test object and set-up **27**
4.1 Specifications of Motor . . . 27
4.2 Inverter . . . 29
4.3 Test bench set-up . . . 29

5 Model Implementation **31**
5.1 Simulation model . . . 31
5.1.1 Dual winding model . . . 32
5.1.2 Simulink implementation . . . 32
5.1.3 Dual model implementation . . . 33
5.2 Fault implementation . . . 34
5.3 Control strategies and implementation . . . 34
5.3.1 Three phase-open fault control strategy . . . 35
5.3.2 Single open-phase fault control strategies . . . 35

5.3.3 Resonant controller 39

6 Results and analysis 43

6.1 Performed tests and simulations 43
6.1.1 Healthy Operation of the dual winding machine 44
6.1.2 Three-Phase Open Circuit 45
6.1.3 Comparison of tests 47
6.2 Single-Phase Open Circuit 48
6.2.1 Lab verified open phase cases 48
6.2.2 Simulated open phase cases 51
6.2.3 Single-Phase Open summary 52
6.3 Balanced Short circuit 53
6.4 Additional performed tests 54
6.5 Resonance controller simulations 54
6.5.1 Healthy dual operation 55
6.5.2 Three-phase open operation 56
6.5.3 Dual winding operation with one phase open 58
6.6 Sustainability Aspects 59

7 Conclusion 61

7.1 Future work 62

Bibliography 65

A Appendix 1 I

A.1 Current equation I
A.2 Dual winding Simulink model II

B Appendix 2 III

B.1 Resonant controller derivation III

1

Introduction

For vehicles and many other applications, permanent magnet synchronous motors (PMSMs) are often chosen by design engineers due to their high performance. For certain applications, high reliability of the drive systems is a desirable attribute, and it is therefore frequently investigated. Machines which are less likely to experience a fault, or those whose performance is not significantly affected by a fault, are attractive from the point of view of productivity, in production lines for an example. Propulsion with electric motors, steering-by-wire, and other similar automated applications require very high reliability both in the software as well as the hardware of the drive system, especially if the safety and comfort of passengers in a vehicle is to be maximised.

Fault tolerance is, therefore, a field of electric motors which has been expanding in for many years and will continue to develop further in the coming years. Approaches to improve the fault tolerance and reliability of drive systems have been developed for the electrical and mechanical parts of the drive; a fault-tolerant design is needed in both the motor itself as well as the power electronics to maintain operational functions in case of a fault occurring, [1, 2, 3].

The PMSM is already a considerable improvement over the electrically excited synchronous machine. It does not require a rotor circuit since the permanent magnets contribute a reliable amount of flux for torque generation. This leaves faults in the machine to occur only in the stator winding. Faults in the converter, on the other hand, typically occur due to power switch failure [4].

One such improvement is in the winding arrangement, which can have a profound impact on the capabilities of the machine in case of a fault. A dual-winding arrangement, in which windings are segregated to opposite sides of the stator and have their own neutral point, is central in this thesis. This configuration essentially splits the machine into two smaller and identical machines and, in case one fails, torque can be produced normally with the other one.

Modelling of PMSM is well documented in literature, as well as fault analysis in electrical machines. The three phase model of a salient PMSM is well known [5], and modelling in the synchronous reference frame, with rotor-fixed dq coordinates is also common. Physical phase-variable modelling using finite element analysis (FEA) to obtain machine parameters was used in [6] for the sake of time-effectiveness as well as increased accuracy in the model. Literature, however, is lacking a study where this method is used to simulate a dual winding PMSM under different fault scenarios. This thesis presents such a study as well as a validation of the model with experimental tests on a prototype motor.

This thesis is performed within the framework of an ongoing design project at Aros Electronics. A FEM model is available for simulation purposes and a prototype is available for bench testing.

1.1 Aim

The purpose of this thesis is to investigate and evaluate the performance and fault-tolerance of a dual three-phase permanent magnet motor designed for high reliability applications. The purpose can be divided in to two main aims.

The first aim is to evaluate the performance of the prototype machine during different fault and operating conditions.

The second aim is to investigate ways to increase the post-fault performance and mitigate the consequences of the different faults that are considered.

1.2 Scope

A simulink model is developed for the first aim and a test-rig, available at Aros-electronics, is utilised for experimental tests. The performance of the machine is evaluated through practical tests and simulations for single and multiple open phase faults, and three post-fault control strategies are compared against the healthy benchmark.

For the second aim, different control approaches are investigated and applied with the focus of not having to add any additional components to the system. This approach is chosen because methods where fault-tolerance and redundancy is increased through various hardware changes are quite common in literature. Non hardware-based approaches are not as prevalent, thereby making it an interesting topic to look in to. Not adding any components to the system also gives the opportunity of quick after-market implementation by only updating the software, as well as keeping down overall costs of the system.

Fault detection, which is a very important functionality of a fault-tolerant drive system, is not specifically investigated in this thesis. Instead the faults are introduced and presumed to be known. More specifically, it is assumed that failures occur in the inverter switches or at the terminals, as well as that the considered faults only affect the inverter legs that are specified. It is also assumed that a failure does not generate another one and that it is possible to isolate any faulty converter leg.

Turn-to-turn faults are not specifically studied in this thesis.

The position of the rotor is assumed to be known in the simulations, and it is obtained with an encoder in the bench tests. Sensorless operation is generally preferred in reliability applications, but is excluded from this work.

Discretization, and therefore modulation, is disregarded in the simulations. The motor is continuously controlled. Furthermore, the dynamic behaviour of the motor is also disregarded, and focus is only on steady state behaviour.

2

Theory

PMSM design can vary greatly depending on its intended application. In the following sections, based academic literature and for the purpose of this thesis, the most relevant aspects of machine design will be discussed.

2.1 PMSM machine design

In permanent magnet synchronous electric machines, typically three phases are coiled on the armature separated from each other an equal distance in space, 120°. Once excited by a three-phase voltage source, whose phases are 120° separated in time, a rotating magnetic field will be produced, and the speed at which it rotates is the synchronous speed. The field in the rotor is produced by permanent magnets and it rotates with the rotor. Since the magnetic poles are attracted to the rotating field created in the armature, the rotor will also rotate at synchronous speed [7].

For a machine with a single pole pair, the machine will rotate once every electric cycle. In the case of multiple pole pairs, each pole will cover 360 electrical degrees, and therefore the machine will rotate once every N_p electric cycles. From this concept follows the relationship between electrical and mechanical position and speed in radians per second, expressed as

$$\theta_e = \theta_m N_p \tag{2.1}$$

$$\omega_e = \omega_m N_p \tag{2.2}$$

where θ is angle, ω is speed, and the subindices m and e indicate mechanical and electrical, respectively.

Reluctance represents the opposition to a magnetic flux, $\mathcal{R} = \frac{F}{\phi} = \frac{Ni}{\phi}$, where $\mathcal{R}$ is reluctance, F is the magnetomotive force, ϕ is the magnetic flux, N is the number of turns in a coil and i is the current in the coil. If magnetic flux is proportional to current in the coil, $\phi = Li$, and current remains constant, it can be said that reluctance is inversely proportional to inductance, L, which represents the ratio between an induced voltage and the current causing it, $V(t) = L\frac{di}{dt}$.

Magnet location has significant influence on the reluctance of the path their magnetic field follows. The relative permeability of the magnets is similar to that of air and much lower than the relative permeability of iron cores. Therefore, permanent magnets mounted on the surface of the rotor offer the lowest reluctance configuration when compared with magnets mounted in the interior of the rotor. The former configuration is considered “non-salient” and the variation of inductance with rotor position is very small compared with the latter, known as “salient”[8].

Assuming magnetic linearity by disregarding saturation, the magnetic coenergy in the motor can be expressed by

$$W_{co} = \frac{1}{2} L i^2 + i\Psi, \tag{2.3}$$

where the first term will be equal to the energy stored in the coupling field provided by the inductance of the machine and the stator currents, and the second term represents the energy provided by the permanent magnets in the rotor. Differentiating the previous expression with respect to the mechanical rotor angle and considering (2.1) yields a general expression for the electromagnetic torque produced by the motor

$$T_e = n_p i \left(\frac{1}{2} \frac{dL(\theta_e)}{d\theta_e} \cdot i + \frac{d\psi_{pm}(\theta_e)}{d\theta_e} \right). \tag{2.4}$$

Ideally, the back emf induced in the coils by the permanent magnets will have a sinusoidal distribution in space. However, magnet shape and their location ultimately determine the shape of this waveform. Additionally, the magnet location leads to a tendency of the rotor to align with the stator in directions where the reluctance is minimized. This tendency is known as cogging torque and contributes to torque ripple in the output of the machine. Careful consideration of magnet location, such as skewing of the rotor considering the specific number of poles and slots in the machine, will reduce such cogging torque and make the back emf waveform more sinusoidal [9].

2.1.1 Windings

Motors with more than one 3-phase sets, called multi-stator machines, typically adopt arrangements of such sets in two different ways: Interlaced subsystems and segregated subsystems. The differences between arrangements will be explained below, inspired from [10].

Interlaced windings

In this configuration of multi-stator machines, coils of one subsystem are next to coils of another subsystem, as shown in figure 2.2. With this arrangement, coils of one winding set are more coupled to other sets in the stator than with the segregated arrangement. Currents in one set will have a stronger effect on currents in other sets. Additionally, phases of each set are evenly distributed in space, which provides smoother operation of the machine under set failure, provided an appropriate control strategy is in place.

Segregated windings

Segregated windings are characterized by individual winding sets that are geometrically separated from other sets in the stator. This provides reduced magnetic coupling between winding sets when compared with interlaced windings, and hence better magnetic isolation. Furthermore, coupling between phases within a winding will not be symmetrical due to their physical position in the stator. The windings configuration can be complicated further by introducing two different winding methods.

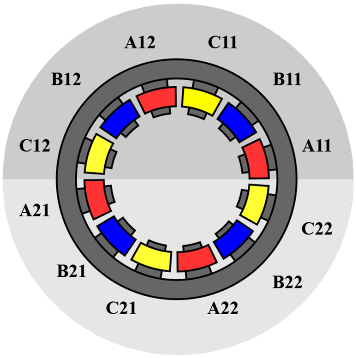
A12
C11
B12
B11
C12
A11
A21
C22
B21
B22
C21
A22

Figure 2.1: Non-overlapping segregated winding

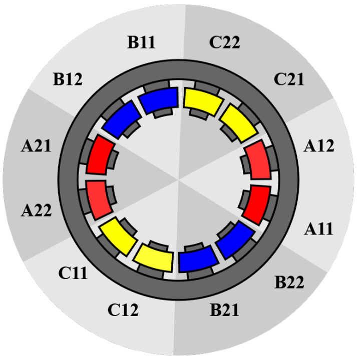
B11
C22
B12
C21
A21
A12
A22
A11
C11
B22
C12
B21

Figure 2.2: Interlaced dual winding

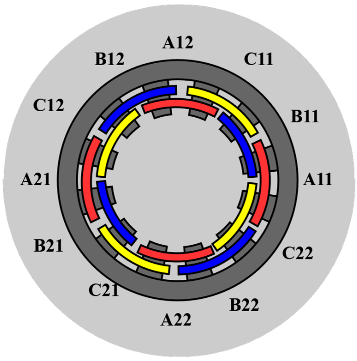
A12
B12
C11
C12
B11
A21
A11
B21
C22
C21
B22
A22

Figure 2.3: Distributed winding

Distributed windings

In this winding arrangement, each coil is wound through slots that are not adjacent to each other. If all slots are occupied, coils will overlap with each other and surround multiple teeth in the stator, as shown in figure 2.3. Depending on if the winding sets are interlaced or segregated, sections of the stator can provide a stronger magnetic coupling between coils of different phases or different subsystems when compared with the non-overlapping arrangement.

Non-Overlapping concentrated winding

Non overlapping concentrated winding arrangements are those that wind each coil in the stator around a single tooth. The advantage of this method is a low mutual inductance between coils. Furthermore, coils in this arrangement that share slots are known as double-layer windings and those that don't share slots are referred to as single-layer windings. The latter further reduces the magnetic coupling between coils.

2.2 Modelling of PMSM machine

Modelling of the machine is based on [11], where computation results from a FEM model are used as inputs into the equation based phase variable model instead of using analytical calculations of these values. This approach was used to obtain accurate values of the self and mutual inductance between phases and winding sets, and also for the reproduction of the EMF generated by the permanent magnets.

The phase variable model of a PMSM proposed in [11, 12] is presented below composed of three phase differential equations for voltage, flux linkage, and the torque and motion equations:

$$\mathbb{V}_{abc} = \mathbb{R} i_{abc} + \frac{d}{dt}\psi_{abc}(i_{abc}, \theta), \tag{2.5}$$

$$\psi_{abc} = \psi_{sabc}(i_{abc}, \theta) + \psi_{rabc}(\theta), \tag{2.6}$$

$$\psi_{sabc}(i_{abc}, \theta) = \mathbb{L}_{abc}(\theta) i_{abc} \tag{2.7}$$

where $\mathbb{V}_{abc}$ are the terminal voltage vectors $[V_a\ V_b\ V_c]^T$, $\mathbb{I}_{abc}$ are the current vectors $[i_a\ i_b\ i_c]^T$, $\psi_{abc}(i_{abc}, \theta)$ the stator flux linkage, $\psi_{sabc}(i_{abc}, \theta)$ the flux linkage produced by stator currents, $\psi_{rabc}(\theta)$ the flux linkage produced by the rotor permanent magnets $[\psi_{ra}(\theta)\ \psi_{rb}(\theta)\ \psi_{rc}(\theta)]^T$, $\mathbb{R}_{abc}$ the resistance matrix, $[r_a\ r_b\ r_c]$, and the inductance matrix

$$\mathbb{L}_{abc}(\theta) = \begin{bmatrix} L_{aa}(\theta) & L_{ab}(\theta) & L_{ac}(\theta) \\ L_{ab}(\theta) & L_{bb}(\theta) & L_{bc}(\theta) \\ L_{ac}(\theta) & L_{cb}(\theta) & L_{cc}(\theta) \end{bmatrix} \tag{2.8}$$

The electromagnetic torque produced is

$$T_m = n_p i_{abc}^T \left(\frac{1}{2} \frac{dL_{abc}(\theta_e)}{d\theta_e} \cdot i_{abc} + \frac{d\psi_{rabc}(\theta_e)}{d\theta_e} \right), \tag{2.9}$$

and the motion equations are given as

$$J\frac{d\omega}{dt} = T_m - B\omega - T_L \tag{2.10}$$

$$\frac{d\theta}{dt} = \omega \tag{2.11}$$

where J is the inertia of the machine ω is the angular speed and equal with the position derivative, B is the viscous damping coefficient, and T_L is the external load torque.

This model is further expanded to include two winding sets, resulting in a double system coupled by an inductance matrix which includes coupling between phases and winding sets:

$$L_{abc1abc2}(\theta) = \begin{bmatrix} L_{a1a1}(\theta) & L_{a1b1}(\theta) & L_{a1c1}(\theta) & L_{a1a2}(\theta) & L_{a1b2}(\theta) & L_{a1c2}(\theta) \\ L_{b1a1}(\theta) & L_{b1b1}(\theta) & L_{b1c1}(\theta) & L_{b1a2}(\theta) & L_{b1b2}(\theta) & L_{b1c2}(\theta) \\ L_{c1a1}(\theta) & L_{c1b1}(\theta) & L_{c1c1}(\theta) & L_{c1a2}(\theta) & L_{c1b2}(\theta) & L_{c1c2}(\theta) \\ L_{a2a1}(\theta) & L_{a2b1}(\theta) & L_{a2c1}(\theta) & L_{a2a2}(\theta) & L_{a2b2}(\theta) & L_{a2c2}(\theta) \\ L_{b2a1}(\theta) & L_{b2b1}(\theta) & L_{b2c1}(\theta) & L_{b2a2}(\theta) & L_{b2b2}(\theta) & L_{b2c2}(\theta) \\ L_{c2a1}(\theta) & L_{c2b1}(\theta) & L_{c2c1}(\theta) & L_{c2a2}(\theta) & L_{c2b2}(\theta) & L_{c2c2}(\theta) \end{bmatrix} \tag{2.12}$$

The torque calculation for the dual winding implementation results as

$$T_m = n_p i_{abc1abc2}^T \cdot \left(\frac{1}{2} \frac{dL_{abc1abc2}(\theta_e)}{d\theta_e} \cdot i_{abc1abc2} + \frac{d\psi_{rabc1abc2}(\theta_e)}{d\theta_e} \right), \tag{2.13}$$

where $i_{abc1abc2}$ is the current vector $[i_{a1}\ i_{b1}\ i_{c1}\ i_{a2}\ i_{b2}\ i_{c2}]^T$, and $\psi_{rabc1abc2}(\theta)$ is the rotor flux linkage vector.

2.3 Inverter theory

Voltage Source Converters are used to transform DC into AC and vice versa. A single-phase full bridge converter is known to have 4 switches whilst a half-bridge, also known as a half-wave converter, only requires two [13]. When the conversion is DC to AC they are referred to as inverters and they are conveniently used to provide power to electric motors since they are fully controllable voltage sources. In simple terms, an inverter amplifies digital signals to create an AC power source from a DC source. There are different topologies used for this purpose, the most common of which is the three-phase inverter. It employs one half-bridge converter per leg, shown in figure 2.4.

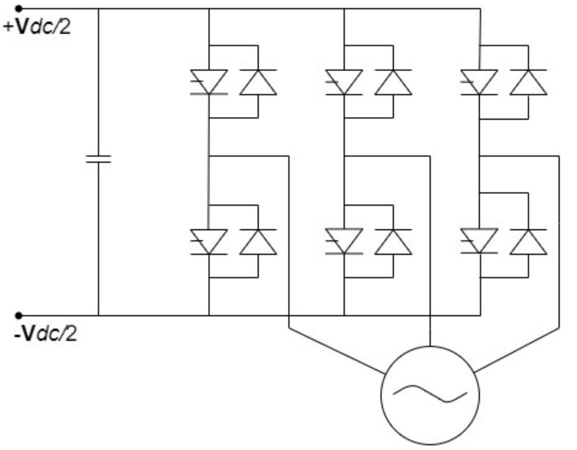

Figure 2.4: Voltage-source inverter and AC machine.

Other topologies may include 4 switches (full bridge) per leg, and a neutral wire connection with or without active switching. The output of the inverter is limited to the available combinations of its switches while avoiding to close both switches in a leg simultaneously. For the inverter shown in figure 2.4, 8 possible combinations exist. Each of these will correspond to a voltage vector in the $\alpha\beta$ coordinate system, as shown in figure 2.5. These combinations can then be chosen using one of several modulation techniques to produce the desired output.

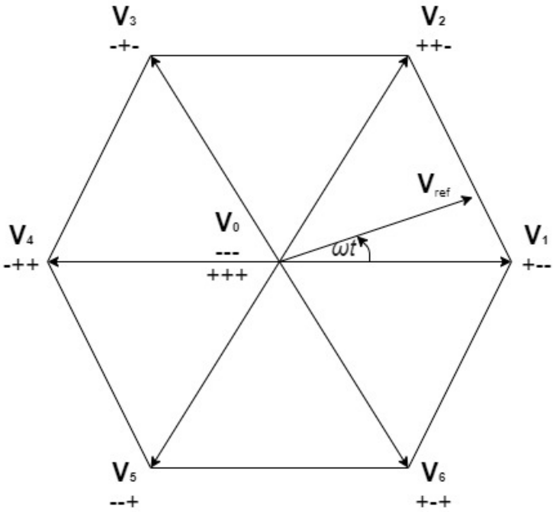

Figure 2.5: Space-vector diagram.

2.4 DQ-transformation

The electrical quantities describing either voltage or current in phase a, b or c, are usually described by three cosine functions phase shifted by 120°. In a three phase system, with a floating neutral point, the generalised quantities can be summed up to zero as

$$x_a + x_b + x_c = 0 \tag{2.14}$$

if no zero sequence is assumed, which is the case if no neutral connection is present. These three quantities can be expressed as the two equivalent α and β quantities by applying the Clarke transformation

$$\begin{bmatrix} x_\alpha \\ x_\beta \end{bmatrix} = K \begin{bmatrix} \frac{2}{3} & -\frac{1}{3} & -\frac{1}{3} \\ 0 & \frac{1}{\sqrt{3}} & -\frac{1}{\sqrt{3}} \end{bmatrix} \begin{bmatrix} x_a \\ x_b \\ x_c \end{bmatrix} \tag{2.15}$$

obtaining the two perpendicular axes shown in figure 2.6. These quantities are often referred to as the real and imaginary axes in the complex plane. The normalised result of transforming the *abc* quantities to $\alpha\beta$ frame is shown in figure 2.7. The K in (2.15) is the scaling constant which can be chosen as to obtain an Amplitude-invariant, Power-invariant or RMS-invariant transformation depending on what is more convenient in the specific case.

As figure 2.6 shows, the $\alpha\beta$ frame as well as the standard *abc* frame, are stationary reference frames. In order to obtain the DC quantities shown in the last section of figure 2.7, the Park transformation is applied as

$$\begin{bmatrix} x_d \\ x_q \end{bmatrix} = \begin{bmatrix} \cos\theta & \sin\theta \\ -\sin\theta & \cos\theta \end{bmatrix} \begin{bmatrix} x_\alpha \\ x_\beta \end{bmatrix} \tag{2.16}$$

thereby moving from the stationary $\alpha\beta$ frame to the rotating dq frame, where the transformation angle θ is the electrical angle. The d and q notation stands for direct and quadrature directions, where the d-axis is defined as the direction of rotor flux and q-axis as leading the d-axis by 90°, as can be seen in figure 2.7. The Clark and Park transformations are extensively used and thoroughly described in literature such as in [14] and [15].

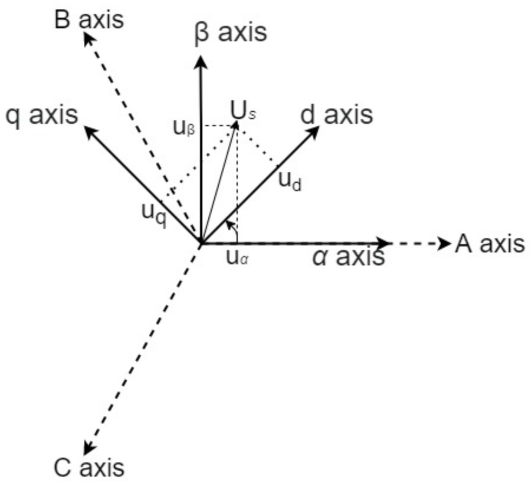

Figure 2.6: Relationship between *abc*, $\alpha\beta$ and *dq* reference frames.

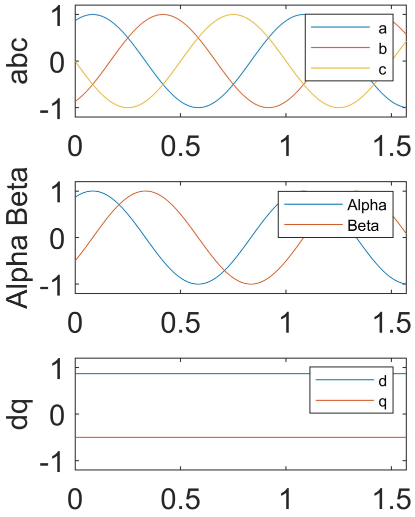

Figure 2.7: Signals in different reference frames using amplitude invariant transformation.

2.4.1 Harmonics

In an ideal three phase system, the three sinusoidal waveforms has no distortions and sum up perfectly at all times. This is however not the case in physical systems. The harmonic distortions of the supply voltage can originate from the mains for grid connected machines or from the inverters and other power electronic devices. The machine itself also represents a nonlinear load caused by such things as air-gap field distortion, asymmetric inductances and distorted back emf [14, 16, 17].

In a symmetric three phase system it can be shown through fourier series expansion that the even-order harmonics disappear due to the half-wave symmetry. With the three phases shifted by 120°, the odd numbered harmonics are all present where the first is the fundamental component. Harmonics that are multiples of three sum to zero due to symmetry and are called the zero sequence components. It can therefore be concluded that the prevailing harmonics are of order 5, 7, 11, 13, 17, 19 and so on, with a decrease in amplitude as the harmonic order increases [14].

When transforming the signals in to the *dq* frame using the Park and Clark transforms the harmonic order also changes. As shown in [17], the 5th and 7th harmonic in the *abc* frame is represented by the 6th harmonic in the *dq* frame, while the 9th and 11th *abc* frame harmonics are the equivalent of the 12th *dq* harmonic. The prevailing *dq* current harmonics continue as multiples of the 6th as, 6, 12, 18, 24 and higher. As is the case for the *abc* domain harmonics the higher orders can however usually be neglected, especially when the motor is operation in the high speed region, as they then are filtered out by the mechanical system [18, 19]. The 5th and 7th order harmonics in *abc* frame have a big impact on the torque ripple but does not effect the average torque significantly [20].

If the system is unbalanced, as in the case of one phase not being connected, the asymmetric inductance leads to a 2nd order harmonic being present in the *dq* axis currents [21]. The presence of the 2nd and higher even-numbered harmonics in the *dq* frame leads to unwanted harmonics in the *abc* frame [22]. Inaccurate estimation of motor parameters, discussed in the next section, can also lead to 2nd order harmonics in the *dq* frame [23].

2.5 Control theory

The transformation from the *abc* to *dq* quantities allow for a PI controller to be implemented, as the three AC quantities are simplified to two DC quantities. Field oriented control (FOC), also known as vector control, is used to control the current, flux and voltage vectors. The control technique decomposes the stator currents as two orthogonal vectors, one representing the magnetic flux and the other the torque production of the motor. As described in section 2.4, the flux is oriented in the d-current direction and the torque in the q-current direction [14].

A speed controller is used which compares the measured speed with the speed reference given. The error signal is used to calculate a torque reference limited by the machines maximum current magnitude. The limited reference torque is then used to calculate the d and q axis reference currents. Since the motor is salient, meaning that the d-axis current also produces torque, a maximum torque per ampere (MTPA) calculation is preformed producing a current angle input to the current reference calculation. The reference currents are fed to the current controllers, which compares them with the measured winding currents, and outputs the needed voltage signal in order to control the speed of the motor [14].

Constant motor parameters are assummed, and the condition to achieve MPTA operation is

$$\frac{\partial T_e}{\partial \beta} = \frac{3}{2} n_p I_s [\psi_m \cos\beta + (L_d - L_q) I_s \cos 2\beta] = 0 \tag{2.17}$$

where β is the current vector angle. The reference value of the angle can therefore be obtained from (2.17) as

$$\beta = \cos^{-1}\left[\frac{-\psi_m + \sqrt{\psi_m^2 + 8(L_d - L_q)^2 I_s^2}}{4(L_d - L_q) I_s}\right] \tag{2.18}$$

If variations of motor parameters are considered, MTPA control is much more difficult to achieve, as explained in [24]. These would be L_d and L_q considering saturation, and ψ_m considering temperature variation.

2.5.1 IMC controller design

The PMSM stator voltages can be modelled in dq-frame as

$$u_{sd} = R_s i_{sd} + L_{sd}\frac{di_{sd}}{dt} - \omega_r L_{sq} i_{sq} \tag{2.19}$$

$$u_{sq} = R_s i_{sq} + L_{sq}\frac{di_{sq}}{dt} + \omega_r L_{sd} i_{sd} + \omega_r \Psi_{pm} \tag{2.20}$$

where R_s is the stator resistance, L_s the stator inductance, ω_r the electrical rotor speed, Ψ_{pm} the rotor permanent flux linkage and subscript d and q denotes respective axis. The $\omega_r L_{sq} i_{sq}$ and $\omega_r L_{sd} i_{sd}$ terms represent the cross coupling between the d and q axis and $\omega_r \Psi_{pm}$ the back emf [14].

By solving (2.19) and (2.20) for i_{sd} and i_{sq} and applying Laplace transformation the electrical transfer functions of the PMSM are obtained. By applying the closed loop current control design strategy, according to internal model control (IMC) described in [14], a PI controller can be derived.

In figure 2.8 the simplest form of the closed loop system block diagram G_{cl} is shown containing the controller F_c, and the machine model G_c. Here subscript c is used for current controller, but the same method is used for the speed controller, then denoted by subscript s.

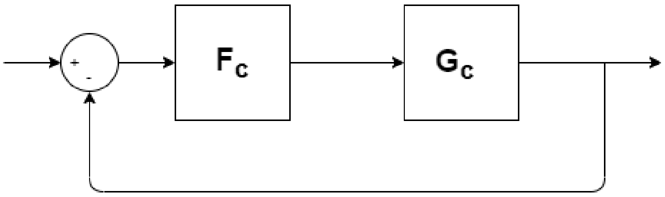

Figure 2.8: Closed loop system block diagram, G_{cl}

By making the G_{cl} a first order low pass filter as

$$G_{cl} = \frac{F_c G_c}{1 + F_c G_c} = \frac{\alpha_c}{\alpha_c + s}, \tag{2.21}$$

where α_c is the bandwidth of the system, the proportional and the integrating parameters of the controller are obtained. The relationship between the rise time and the bandwith of the system is

$$\tau = \frac{ln(9)}{\alpha_c} \tag{2.22}$$

where the rise time is defined as the time from 10% to 90% of the step response time.

In order to improve the disturbance rejection of the controller active damping, anti-windup and feed-forward of the disturbance is applied. The PI controller parameters then becomes

$$k_p = \alpha_c \hat{L}_{sx},\ k_i = \alpha_c k_p,\ R_{ax} = \alpha_c \hat{L}_{sx} - \hat{R}_s \tag{2.23}$$

where R_a is the active damping term and $\hat{L}_{sx}$ represents $\hat{L}_{sd}$ or $\hat{L}_{sq}$ giving the gains for both of the respective current controllers. The hat signs over the variables indicate estimated values used by the controller. Perfect estimation and disturbance cancellation is presumed during the control design.

The plant model G_c is for the control design purpose considered ideal, later however, the actual plant model it controls is derived in section 5.1 and 5.1.1 and implemented i Simulink in section 5.1.2.

The speed controller is cascaded outside the inner current control loop, which is considered infinitely fast for derivation purposes. Ideally the speed and current control bandwidths should have a relation of

$$\alpha_c \cdot 10 > \alpha_s \tag{2.24}$$

in order for the speed controller not to be affected by the current controller. The speed controller is derived using the same steps as for the current controller and active damping and anti-windup is implemented in the same way.

3

Fault tolerant drive systems

This section presents how fault tolerant machines are defined in available literature. A review of the different possible fault that can occur in a PMSM and its accompanying power electronic components is performed. Different suggested methods of fault-tolerant designs and post-fault control strategies are also presented.

Fault tolerant drive systems are defined in [25] as a system fulfilling the following criteria:

- Partitioning and redundancy
- Isolation between units
- Fault detection and reporting
- Continued operation until the next service opportunity

In [26] it is elaborated on how the first two points can be achieved either by increasing the number of machine units, increasing the number of phases, or implementing a dual-winding. It is also emphasised that, depending on the various faults the machine is required to tolerate, different machine configurations can be utilised.

The meaning of fault-tolerance can further be divided, as in [4], into either a system that is designed to reduce the number of occurring faults, or a system with post-fault performance capabilities. In the case of post-fault capabilities two approaches can be chosen. Either having redundant components where in case of fault, a healthy component is available for the same task, or a configuration where the remaining healthy components can be controlled to still be operational.

Depending on application requirements, fault tolerant machines can be designed to have a continuous post-fault operation capability, or a more limited short-term operation capability. Various combinations of controllable post-fault systems and systems with redundant components can be combined to achieve desired level of post-fault performance. The terminology to distinguish between a fault-tolerant and a redundant systems is not standardised in literature and the approaches often overlap [4]. The reliability of the drive is improved through redundant design and fault-tolerant control in [3] and [27, 28].

3.1 Possible faults

Post-fault functionality of an electric drive system depends on the type of fault that has occurred and its severity, which in turn depends on the design of the drive itself. This section describes possible faults in the machine and converter, and their possible consequences, disregarding possibilities of a DC-bus failure.

3.1.1 Winding short-circuit Faults

Conductors inside a machine are wound several times around each stator tooth and, depending on winding design, the wires from different phases can also be in contact with each other and with the machine stator. Winding insulation failure can therefore cause a short between different parts of the machine, as mentioned in [29]. When the insulation on these wires breaks down, a path for current to flow will be created and its effects will depend on the location of the breakdown. Reasons for winding insulation failure, such as thermal and electric stress, are also described in [29].

One common location for the insulation to fail is between one or more turns around a tooth short, creating what is known as a turn-to-turn short circuit fault. This type of short can cause a current higher than rated to be induced inside the damaged coil and excessive heat produced by this current will eventually cause degradation of the insulation in the neighbouring turns. Even though this single turn-to-turn fault is a small part of the winding it will eventually lead to more turns being shorted, resulting in larger currents and heat in the stator. In [29], the author mentions this as one of the most severe types of faults since they are difficult to detect when they occur and impossible to remedy without replacing the winding since the currents will be induced in the loop whenever the machine is rotating.

Other possible short circuit faults in the stator circuit are those between phases or between a phase and ground. The former can only occur if coils or wires of different phases are in contact, and the latter may cause damage to the mechanical structure of the stator. Unbalanced faults are those that short a current path between two of the phases, and a balanced fault shorts all three phases together. In both balanced and unbalanced faults, currents are induced while the machine is rotating and are accompanied by a breaking torque.

Balanced Short Circuit Fault

From [30], the induced short-circuit currents for a balanced fault is expressed as a function of speed as

$$\begin{bmatrix} Id_{sc} \\ Iq_{sc} \end{bmatrix} = -\frac{1}{R_s^2 + \omega^2 L_d L_q} \begin{bmatrix} \omega^2 L_q \psi_{pm} \\ \omega \psi_{pm} R_s \end{bmatrix} \tag{3.1}$$

and the current magnitude as

$$|I_{sc}| = \frac{\sqrt{(\omega^2 L_q \psi_{pm})^2 + (\omega \psi_{pm} R_s)^2}}{R_s^2 + \omega^2 L_d L_q} \tag{3.2}$$

The breaking torque is expressed as

$$T_{brk} = -\frac{3}{2} npR_s \psi^2 \omega \frac{R_s^2 + \omega^2 L_q^2}{(R_s^2 + \omega^2 L_d L_q)^2} \tag{3.3}$$

From these equations it is notable that the short circuit current increases with speed and approaches ψ_{pm}/L_d, as indicated in [27, 30], while the maximum breaking torque and the speed at which it occurs are a function of the saliency ratio [30]. This is illustrated in figure 3.1

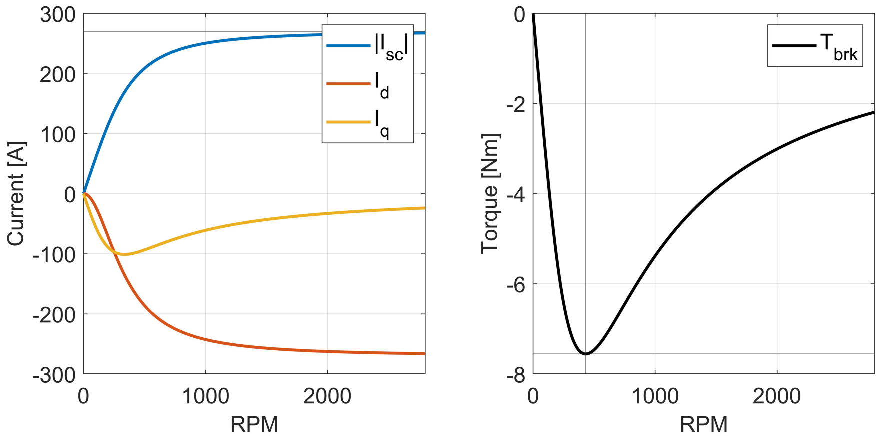

Figure 3.1: Behaviour of current and torque during a three phase short circuit.

In the case of a dual winding machine, operation under a three phase fault is theoretically possible if the machine is appropriately designed. This would be with a large L_d in proportion to ψ_m. Furthermore, in a dual machine, a short between windings is also possible and its likelihood depends on the winding arrangement. Although some of the faults mentioned in this section might be tolerable, they cannot be remedied once they occur unless the winding or faulty inverter leg is replaced.

3.1.2 Open phase faults

Open circuit faults are typically a result of physical damage to the machine, or to the conductors between the machine and the converter. In the case of a single conductor being disconnected, the remaining phases may still retain functionality if an adequate control strategy is implemented. This fault can also occur if one or several of the inverter phase legs is purposely isolated.

In the case of a single open phase, phase A for example, there is only one remaining path for the current and the only possible voltage is between terminals B and C. This is under the assumption that there is no neutral point connection, which means that the phase voltages loose any practical use. V_{bc} therefore can only change in magnitude and direction but cannot rotate. As mentioned in [31], this configuration has consequences on the possible torque production of the machine, since the voltage vector is perpendicular to the flux at only two instants.

In the case of a three-phase disconnection, voltages dependent on speed will be induced on the terminals of the winding and pose a risk if they are exposed. A drive system where the machine and inverter are enclosed in the same case makes this type of fault unlikely. If a three-phase disconnection or three-phase inverter failure occurs in a dual winding machine, torque can still be produced from the healthy winding.

3.2 Fault mitigation approaches

3.2.1 Fault tolerant machines

The machine that is the focus of this report is a two segment-three phase winding PMSM, correlating to the segregated winding described in section 2.1.1. This makes it inherently fault-tolerant due to its double winding layout where one winding-set can output torque if the other fails. Thereby three phase open-fault operation is possible by design, albeit at a reduced torque output if rated current is applied.

In case of phase-open fault, the main method described in literature is to increase the fault-tolerant abilities by utilising a neutral connection [22, 32]. This gives an increased possibility to control the remaining phases, and a maintained torque output reduced by $1/\sqrt{3}$, when operated at rated current for the affected winding. The neutral connection needs to be dimensioned for a current magnitude increased by $\sqrt{3}$ of nominal in this case [33]. In order to maintain the rated torque with this configuration, the currents needs to be increased by $\sqrt{3}$ and the neutral by a factor of 3, thereby requiring the hardware affected to be redimensioned accordingly.

Copper losses in the windings naturally increase when currents are increased. The calculation for these losses, per phase, is

$$P_{cu} = I_{rms}^2 R_{ph} \tag{3.4}$$

where I_{rms} and R_{ph} are the effective phase current and phase resistance, respectively.

Stator winding turn-to-turn short-circuit faults are an especially severe type of fault in permanent magnet machines due to the rotors continued excitation of the stator during maintained operation. Therefore winding arrangements that reduce the probability of these faults to occur, as discussed in [34], and fast detection methods mentioned in [35], are the common measures employed. Also by designing the machine with this type of faults in mind, configuring the rotor magnet flux linkage and the inductance saliency ratio, it is possible to minimize the effects of these faults [27].

Finally, the machine can be designed to tolerate a 3-phase short circuit if the design parameters of the rotor are taken into account. The maximum current in this scenario approaches ψ_{pm}/L_d, as discussed in section 3.1.1, so a machine designed with this taken into consideration can therefore limit the current to a desired value.

3.2.2 Fault tolerant Inverters

The most common approach to increase the fault tolerance of inverters are by adding a redundant leg in the converter [36, 37, 38]. If a neutral connection is available the two most common topologies are shown in figure 3.2 and 3.3. In the case when the neutral is connected to the fourth leg, as in figure 3.2a, a rotating magnetic field can be maintained by controlling the neutral point voltage. If the neutral is connected to the dc mid point of the converter, as shown in 3.2b, the capacitors will have to be sized for the large neutral current. The excitation of remaining two phases can be done by controlling the switches in the two remaining converter legs [33, 37].

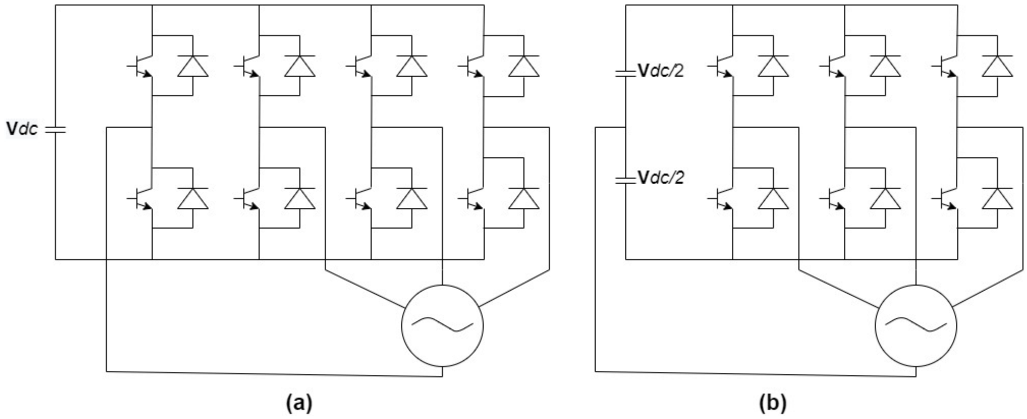

Figure 3.2: Fault-tolerant converter topologies with neutral connection.

In [38] a fault tolerant topology without neutral connection is also discussed shown in figure 3.3. In this case isolating thyristors are implemented to isolate the faulty converter leg which then is replaced by the redundant leg in the converter. In [28] and [39] similar topologies are analysed as in [38] but instead fuses are used to isolate the faulty inverter leg.

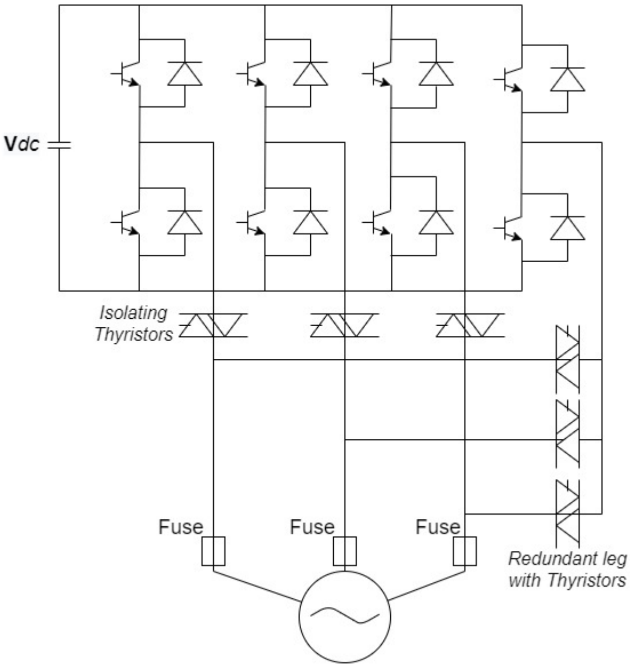

Figure 3.3: Fault-tolerant converter inverter with isolating thyristors and fuses.

If a very high level of fault tolerance and post fault capability is needed, every phase can be connected to its own H-bridge, as discussed in [40]. The system described is a 6-phase modular permanent magnet machine where every H-bridge is connected to its own power source. If one of the phases experiences a fault, it is simply disconnected and the machine keeps operating as a 5-phase machine. Different types of converters for dual-winding motors are covered in [41, 42, 43]. These however employ a design where one main board supplies both winding sets. It is also possible to run the machine with two 6-phase converters, but since this report focuses on a layout with 3-phase converters, this is not further elaborated on.

It is important to keep in mind the added cost of any fault-tolerant topology, as it may add to the over all system cost. As it is concluded in the cost survey in [44], a certain approach and topology might be beneficial for one application but not add much value to another depending on the required post-fault capability.

3.2.3 Post-fault control methods

A wide range of post-fault control strategies are available in literature depending on the faults analysed and topologies used. Two distinguishable sub-groups can be identified. One that focuses on maintaining the same performance capabilities as during healthy operation. Usually reliant on additional hardware being implemented, such as including neutral connections, redundant converter legs, fuses or isolation switches, or independent H-bridge converters for every leg, as covered in section 3.2.1 and section 3.2.2. Designs with full mechanical redundancy, where dual windings are dimensioned to be able to deliver the full rated torque independently, also falls under this category. The other sub-group focuses on remedial post-fault strategies that mainly tries to mitigate the effects of the fault. Usually by implementing control strategies that allow for a continued operation of the machine at a reduced performance. Dependent on type of fault, detection and isolation measures are usually also needed.

Maintained performance strategies

When adding a neutral connection, as mentioned in section 3.2.1, it is possible to maintain the torque output if the current magnitudes are increased for open-phase faults. This also requires the additional change to the control algorithms of changing the reference voltages by 30°. A field oriented controlled machine with space vector modulation is purposed in [45] showing good performance where a neutral is the only additional hardware. In [22] a similar method is stated to preform well under open-loop and V/Hz control but have a poor performance during closed loop control. Therefore a PI controller with an adaptive resonance part is proposed that suppresses the 2nd and 4th harmonics. This increases the tracking capabilities of the PI controller and thereby reducing torque and speed ripple.

Paper [12] also investigates open-phase faults. It utilises a neutral wire, combined with a fourth inverter leg, and introduces a novel transformation matrix which allows for the same PI controller to be used during both healthy and faulty operation.

This allows the two remaining phases to output the same dq-axis control signals and maintain the same torque output in post-fault as in healthy operation.

For dual-winding machines the same PI controllers are widely used as for conventional 3-phase machines. Different methods of handling the mutual influence between the two sets of windings and reducing torque and speed ripple are found in literature. In [46] a sliding mode control combined with a normal PI controller is analyzed. This method increases the dynamic response and makes the controller insensitive to parameter variations and external loads. Fault-tolerance is however not addressed specifically.

The two most common control strategies for dual-winding machines are in [47] and [21] presented as Vector space decomposition(VSD) and two-individual current control. VSD treats the machine as one 6-phase machine while the individual current control treats it like two separate 3-phase machines. [47] concludes that the individual current control has practical benefits compared to the more complex VSD-control, but that it might have instability issues. However it concludes that if the mutual coupling between the two sets of winding is not too strong, the performance is equivalent of that of the VSD-control.

Remedial strategies

The simplest way to continue operation in case of a fault for a dual winding layout, either in the winding or converter, is simply to switch one converter off and continue operation at 50% with the healthy one. However, more performance is of course desirable.

In paper [48] a dual winding machine with isolated neutral points is supplied by two current source inverters. By using field oriented control, and in case of a open-phase fault, a control scheme where the healthy winding generates the opposite torque oscillation as the faulty one, the torque output can be kept constant.

The operation under single- and two-phase open-circuit faults of a dual-winding machine is investigated in [21]. The two Y-connected winding-sets neutral connections are connected in the proposed topology. A VSD-control method is developed combined with a resonant controller to suppress specific dq-current harmonics, arising from the unbalanced operation. A feed forward method is also compared to the resonant controller when used to handle the post-fault 2nd order harmonics in the *dq* frame. It is concluded that the resonant controller is the more robust and adaptable solution and works well as a post-fault controller for the machine.

A method of fault severity estimation, to make it possible to continue operation after a turn-to-turn fault, is developed in [49]. The focus is to minimize torque ripple, and maximize the post-fault torque output, by re-configuring a FOC with the proposed fault-estimation control.

In [50] and [31] similar methods are developed for conventional 3-phase PMSMs. Both look in to the possibility of continued operation after an open-phase fault with the goal of not having any additional hardware added to the system. A Direct Torque control is used in [31] while [50] focuses on FOC, but also compares the performance of the developed post-fault algorithm when DTC or PTC(predictive torque control) is applied. The approach is to utilize the four remaining switches in the healthy inverter legs to control the two active and two zero voltage vectors available in this operation mode. To compensate for lag in the stator current commutation, a "pre-firing" method of the switches is employed to counteract breaking torque that is the result of the abrupt switching action. Both papers report an average post-fault torque output of over 75% of reference value. Two drawbacks of this method are the inability to start the motor again once stopped as well as inability to operate in the field-weakening region. The obvious advantages being that the only change to the system is the modification of the control algorithm, making it very cost efficient.

4

Test object and set-up

This chapter presents the prototype motor available, the inverters used and the lab set-up used for verification of the model and evaluation of the machine.

4.1 Specifications of Motor

The motor prototype this thesis is based on is a two-segment three phase PMSM. The stator windings are divided into two independent Y-connected sets where each set has two parallel coils per phase. There are no neutral wires and the two neutral points have no physical connection. The winding arrangement is shown in figure 4.1 where the first set is represented by the parallel branches A1//A2, B1//B2 and C1//C2, while the second is represented by A3//A4, B3//B4 and C3//C4. The corresponding wire connections for each coil are shown in figure 4.2.By connecting A, B and C terminals together the machine can be operated as a conventional three phase machine with corresponding motor parameters presented in table 4.2.

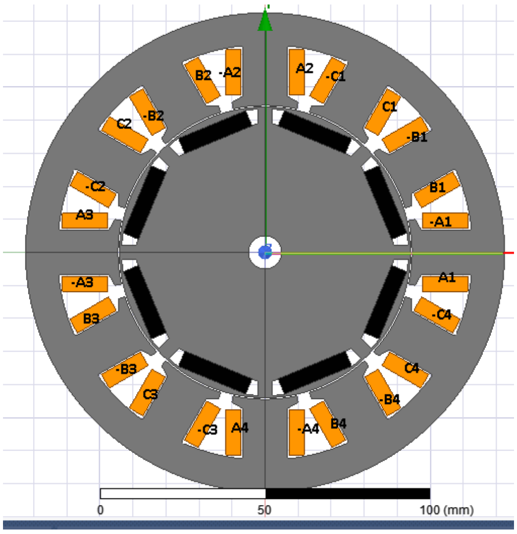

Figure 4.1: Cross section of machine.

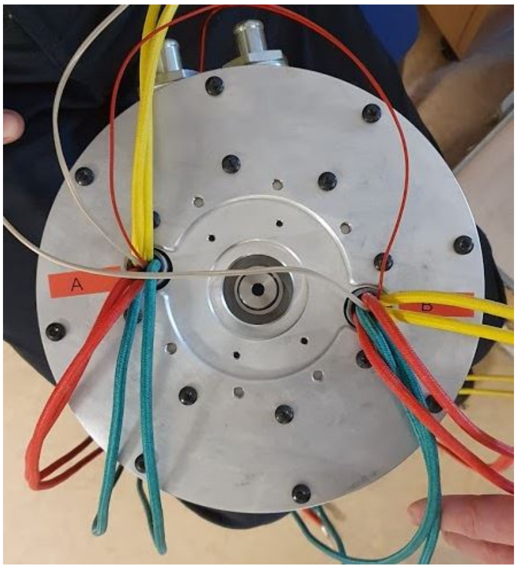

Figure 4.2: Winding connections.

The maximum continuous RMS current allowed per phase is 121.8A, when the machine is connected as a three phase machine, with four parallel coils per phase. In the dual winding configuration, this value changes to 61.9A per phase, since there is now only two parallel coils in each phase.

From figure 4.1 it is clear that the two winding sets occupy one half of the stator each, making it a segmented winding arrangement. The same figure shows the 12 slot stator design with a diameter of 145 millimetres and a rotor length of 45 millimetres. The rotor is skewed in order to reduce the torque ripple due to cogging, as well as the ripple during loaded operation.

Parameter Measurement

Parameters of the machine are measured to verify FEA calculations and to use more accurate values in the simulations. The measured values for the 3-phase connection and dual 3-phase connection, which are the values used in the model, are presented in table 4.1. Theoretical motor parameters from FEM simulations of the 3-phase connected machine are presented in table 4.2, along with other relevant design parameters.

Phase resistance is measured from phase A to phases BC connected in parallel. The measured value is equal to 3/2 of the actual, per phase value, and shows a small difference when compared with the FEA values. The difference is expected since the FEA does not include the connection wires.

Additional wire extensions are used on each phase to facilitate disconnection of one of the phases from the inverter, and to reduce the total number of wires through the current sensor on each inverter leg. The additional resistance is 0.45mΩ and is included in the values shown in table 4.1.

Table 4.1: Measured motor parameters for dual winding connected machine

Motor Parameters				
Parameters	Symbol	Value (1x3ph)	Value (2x3ph)	Unit
Phase resistance	r_{ph}	3.23	5.94	mΩ
D-axis inductance	L_d	14.86	32.53	μH
Q-axis inductance	L_q	27.53	56.83	μH

Inductance is measured in the same way as resistance, and the rotor is turned to find the minimum and maximum values of inductance, which are 3/2 of the L_d and L_q respectively. To obtain the permanent magnet flux linkage ψ_m, the induced voltage is measured at the terminals of the machine with the oscilloscope mentioned on table 4.4. In this measurement, the machine is spun at a certain speed and the PM flux linkage results as $\psi_m = \frac{V}{\omega_e}$, where ω_e is in radians per second. The obtained value is the same for both machine connection configurations.

Table 4.2: Theoretical FEM motor parameters for three phase connected machine

Motor Parameters			
Parameters	Symbol	Value	Unit
Rated mechanical speed	Ω_r	2800	rpm
Rated power	P_{nom}	2.785	kW
Number of pole pairs	n_p	4	-
Phase resistance	r_{ph}	1.6	mΩ
D-axis inductance	L_d	14	μH
Q-axis inductance	L_q	28	μH
Permanent magnet flux linkage	Ψ_m	0.0096	Wb
Rated voltage	$V_{LL_{peak}}$	24	V
Rated current	$I_{rms_{nom}}$	122	A
Max. current for 3 minutes	$I_{rms_{max}}$	269	A
Rated torque	T_{nom}	9.5	Nm
Max. torque for 3 minutes	T_{max}	21	Nm
Torque constant	K_t	0.078	Nm/A
Inertia	J	0.002	kgm^2

4.2 Inverter

The inverters used are shown in figure 4.3 where two inverter are stacked on top of each other in order to supply one winding each. The DC voltage input is rated at 24 volts and the current is limited by the inverters.

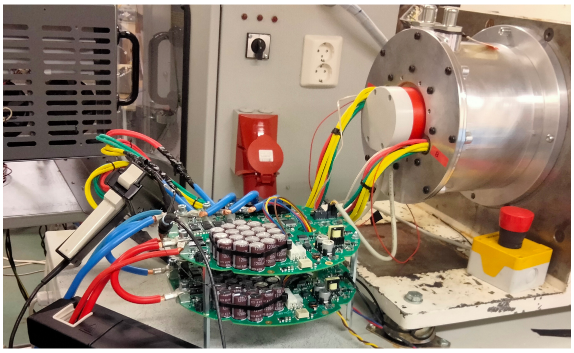

Figure 4.3: Dual inverter used in lab setup.

The encoder used is also visible in figure 4.3, as are some of the measurement instruments.

4.3 Test bench set-up

The motor is mounted on a constant speed test setup to perform the experiments. An additional machine is mechanically coupled to the test object and is controlled by a separate converter. The additional machine can keep the speed constant independently of the torque produced by the test object, since it is rated for higher speed and power than the prototype. The ratings are shown in table 4.3.

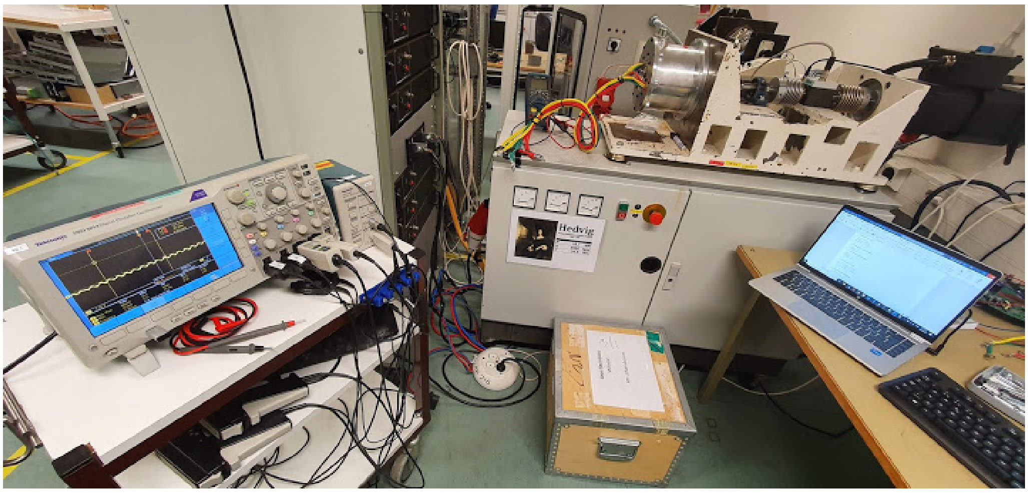

Figure 4.4: Test-bench lab setup.

Devices used to measure voltages, currents and torque are all listed in table 4.4. In figure 4.2 the wiring for the temperature sensors, placed in the end windings, are also visible. The test object is liquid cooled and the connections can be seen at the top of the motor in the same figure.

Table 4.3: Parameters of the additional motor.

Rating		
Power	10.2	[kW]
Speed	4500	[RPM]
Torque	34.5	[Nm]

Table 4.4: Devices used to perform parameter measurements.

Measurement equipment	
Oscilloscope	Tektronix DPO3014
Current clamp AC	Tektronix TCP404XL
Current clamp DC	Tektronix TCP 0150
Torque transducer	HBM T20WN
LCR Meter	GW Instek LCR-6100

5

Model Implementation

The derivation of the mathematical model and Simulink implementation of machine model and controllers are described in this chapter.

5.1 Simulation model

The widely used dq-machine model, mentioned in section 2.5.1, is not suited for implementing and simulating faults. It also does not take the non-ideal inductance and back-emf in to account. The finite element-model models these effects accurately but is instead time consuming. Therefore the physical three phase machine model, suggested in [6] and [11], based on the equations introduced in section 2.2 is implemented. By rewriting (2.5) on line-to-line form and applying Kirchhoff Current Law

$$i_a + i_b + i_c = 0 \tag{5.1}$$

at the Wye-point connection, the line-to-line voltage equations are obtained as

$$\begin{bmatrix} V_{ab} \\ V_{bc} \end{bmatrix} = \begin{bmatrix} r_a & -r_b \\ r_c & r_b + r_c \end{bmatrix} \begin{bmatrix} i_a \\ i_b \end{bmatrix} + \frac{d}{dt} \begin{bmatrix} \Psi_a - \Psi_b \\ \Psi_b - \Psi_c \end{bmatrix} \tag{5.2}$$

Then (2.6) and (2.7) are substituted in to (5.2) and the obtained $\frac{d}{dt}(\mathbb{L}_{ab}(\theta)i_{ab})$ term is expanded with the chain rule in order to solve for the state equations $\frac{di_a}{dt}$ and $\frac{di_b}{dt}$. For the purpose of utilising look-up tables in the simulation, the obtained flux derivative term is rewritten as

$$\frac{d\Psi_r}{dt} = \frac{d\Psi_r}{d\theta} \cdot \frac{d\theta}{dt} = \frac{d\Psi_r}{d\theta}\,\omega \tag{5.3}$$

to make it speed dependent instead of time dependent. On matrix form the obtained equation, when solved for the state equations, can be expressed as

$$\frac{d}{dt}\mathbb{I} = \mathbb{L}^{-1}(\mathbb{V} - \mathbb{R}\mathbb{I} - \omega\frac{d}{d\theta}\mathbb{L}\mathbb{I} - \omega\frac{d}{d\theta}\psi) \tag{5.4}$$

where the inductance matrix on line to line form becomes

$$\mathbb{L} = \begin{bmatrix} (L_{aa} - L_{ac} - L_{ba} + L_{bc}) & (L_{ab} - L_{ac} - L_{bb} + L_{bc}) \\ (L_{ba} - L_{bc} - L_{ca} + L_{cc}) & (L_{bb} - L_{bc} - L_{cb} + L_{cc}) \end{bmatrix} \tag{5.5}$$

Equation (5.4) combined with (2.11), expressing the electrical speed and position, constitutes all quantities needed to express the electrical part of the machine model. The state variable of i_c is calculated from (5.1) as it is needed in the torque calculation in (2.9).

Finally (2.10), combined with (2.9), is used to express the mechanical part of the machine model and calculate the electromagnetic torque.

5.1.1 Dual winding model

In order to model the dual winding layout of the motor in question, the same method as in section 5.1 is used. By applying the inductance table introduced in (2.8) and doing the same steps as in the previous section, but designating two versions of (2.5) as V_{abc_1} and V_{abc_2} to account for both windings sets, a new version of (5.2) is obtained as

$$\begin{bmatrix} V_{ab_1} \\ V_{bc_1} \\ V_{ab_2} \\ V_{bc_2} \end{bmatrix} = \begin{bmatrix} r_a & -r_b & 0 & 0 \\ r_c & r_b + r_c & 0 & 0 \\ 0 & 0 & r_{a_2} & -r_{b_2} \\ 0 & 0 & r_{c_2} & r_{b_2} + r_{c_2} \end{bmatrix} \begin{bmatrix} i_{a_1} \\ i_{b_1} \\ i_{a_2} \\ i_{b_2} \end{bmatrix} + \frac{d}{dt} \begin{bmatrix} \Psi_{a_1} - \Psi_{b_1} \\ \Psi_{b_1} - \Psi_{c_1} \\ \Psi_{a_2} - \Psi_{b_2} \\ \Psi_{b_2} - \Psi_{c_2} \end{bmatrix} \tag{5.6}$$

Continuing the steps with the expanded set of equations gives a new version of (5.4), expressing the current state equations for the dual winding machine, now as $\frac{di_{a_1}}{dt}$, $\frac{di_{b_1}}{dt}$, $\frac{di_{a_2}}{dt}$ and $\frac{di_{b_2}}{dt}$. The i_{c_1} and i_{c_2} currents are then calculated as in section 5.1.

The torque calculation is also done in the same way as in the previous section, but with the vectors and matrices in (2.9) expanded to account for all phases from both sets of windings, resulting in (2.13).

The expanded equations become quite lengthy but an example of the current state equation for the dual winding machine model is shown in appendix A.1. The line-to-line dual-winding inductance matrix is also included.

5.1.2 Simulink implementation

A three phase model is initially implemented, using the parameters from table 4.1, in order to simulate and analyse control methods on a three phase connected machine as well as for verification purposes.

The electrical part of the three phase connected PMSM implemented in Simulink is shown in figure 5.1. The inputs to the block are the line-to-line voltages and the electrical speed and position. Since an encoder is used in the lab set-up the position is presumed to be known and no position estimation is preformed. The outputs of the block are the currents i_a, i_b and i_c.

Subsystem 1 in figure 5.1 represents the inverted inductance matrix, dependent on the electrical angle, in (5.4) and subsystem 2 the resistance matrix. Subsystem 3 represents the electric-speed dependent inductance matrix term, and finally subsystem 4 the speed dependent magnetic flux term, representing the back-emf produced in the machine. Subsystem 1, 3 and 4 utilises look-up tables acquired from the FEM-model of the system. However, skewing of the rotor is not accounted for in the FEM-model, therefore the back-emf look up table output is reduced by 10% to account for this. This makes it possible to model the non-ideal behaviours that a *dq*-model does not take in to account, but still allows for a fast simulation time. In the right hand side of figure 5.1 it can be seen how the current state variables are integrated and the i_c current is calculated according to (5.1).

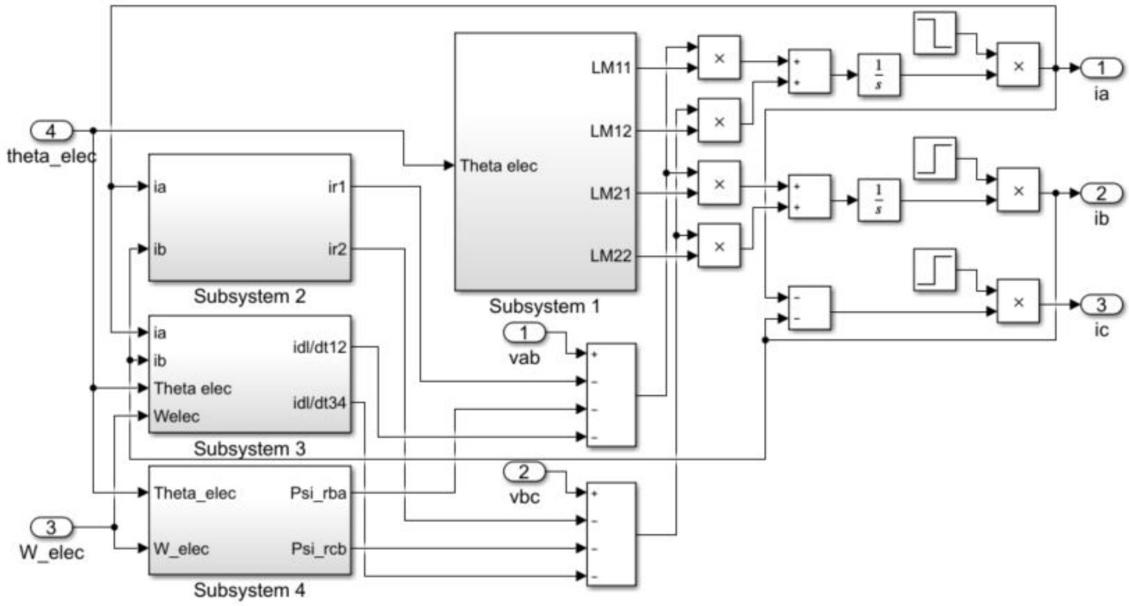
4
theta_elec
ia
ib
ir1
ir2
Subsystem 2
ia
ib
Theta elec
Welec
idl/dt12
idl/dt34
Subsystem 3
Theta_elec
W_elec
Psi_rba
Psi_rcb
Subsystem 4
3
W_elec
Theta elec
LM11
LM12
LM21
LM22
Subsystem 1
1
vab
2
vbc
1/s
1/s
1
ia
2
ib
3
ic

Figure 5.1: Line-to-line three phase electrical machine model.

The torque calculation is implemented in a corresponding fashion as in figure 5.1 based on (2.9). Lookup tables based on the FEM-model are used also in this case in order to account for the non-idealities when calculating the inductance and flux terms.

5.1.3 Dual model implementation

Implementing the dual winding machine is performed as in section 5.1.2 but with the expanded equations from section 5.1.1. The Simulink layout is the same as in figure 5.1 but expanded to account for the additional equations. The expanded equations allow for simulations to include all the mutual couplings between coils in (2.12). These couplings are visualised for one cycle in figure 5.2.

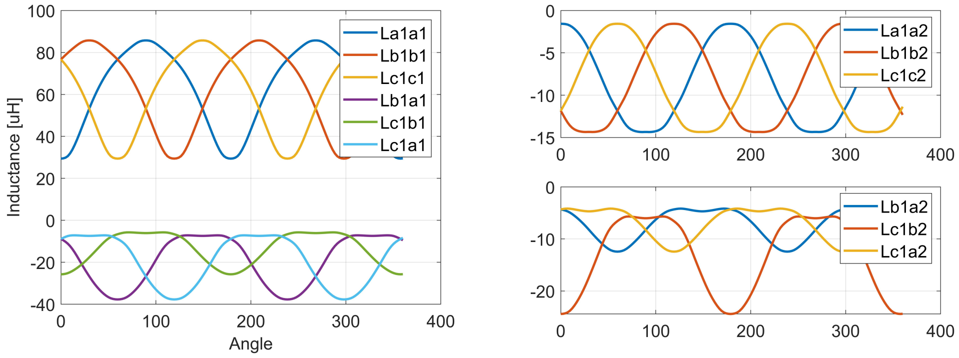

Figure 5.2: Self and mutual inductances within each winding and between each other.

The dual winding parameters from table 4.1 are initially used and the expanded (2.13) is used to calculate the torque. An example of the dual-winding Simulink layout is shown in appendix A.2.

5.2 Fault implementation

To the right, just before the outputs in figure 5.1, three step functions and multiplications blocks are shown. They are used to implement the open phase faults by multiplying the outputs with zero. In the case of one phase open the faults are introduced at the currents zero crossing in order to reduce transient behaviour. Additional step functions are implemented on the input voltage signals in order to force relevant voltage terms to zero when simulating open-phase faults in the inverter. The other relevant terms in the current equations are forced to zero when the phase current goes to zero, which can be seen in equation A.1 in the appendix. To simulate the case of a three phase open fault, that is if a whole inverter looses power, all three step functions are applied.

5.3 Control strategies and implementation

For the healthy machine operation, FOC with PI controllers designed according to IMC, described in section 2.5 are used. For the dual winding connected machine, the two-individual current control approach, discussed in section 3.2.3, is applied.

A speed controller, as described and designed in 2.5, is used in all cases and, as mentioned in section 5.1.2, the position is presumed to be known in the simulations as an encoder is used in the lab set-up. The position of the rotor is therefore obtained directly from integrating the electric speed and used as controller input.

To switch between the standard controller for healthy operation, and the different post-fault control algorithms, the controllers are run in parallel in Simulink and step functions are implemented, similarly to the fault implementation, in order to choose which control signal to use. In other words, the healthy control is switched to the post-fault control at the time of the fault, and therefore assuming perfect fault detection.

5.3.1 Three phase-open fault control strategy

If an entire converter is lost, or if the best way to mitigate a fault is to shut one converter completely off, the other keeps operating with its existing controller. No additional control algorithms are used. By utilising the inherent redundancy of the dual winding layout, 50% torque output can then theoretically be maintained by the healthy winding at nominal current. The alternative is if the machine should keep the same torque output as in the healthy case, a current of twice the magnitude is expected, thus an oversized inverter is needed.

5.3.2 Single open-phase fault control strategies

Open-phase faults are the single most common type of faults in machine drive systems according to [12], constituting 38% of all fault occurrences. Therefore this fault scenario is the main scenario investigated. Two methods of post-fault control is implemented and evaluated in the case of a one-phase open fault.

Method 1 -Prefire

Under remedial strategies in section 3.2.3, the modified FOC algorithm proposed in [50] is introduced. Since this method adheres to the aim of not having to add any extra hardware, it is implemented and evaluated. The main difference between the machine in [50] and the one used in this thesis being the dual-winding layout.

Assuming phase A is lost, only two active voltage vectors are now available oriented in 90°and 270°. The two remaining phases are therefore the equivalent of one remaining phase where the current can be either positive or negative. The only quantities that can be controlled are then the sign and the magnitude. [50] suggest the new torque relationship

$$T_{elec} = i_s \sqrt{3} n_p \psi_{pm} \cos\left(\theta_{elec}\right) \tag{5.7}$$

to calculate the new current reference, that is implemented in the $\alpha\beta$ frame of reference.

When solving for the current in (5.7) the cosine function causes the current to be infinite when the angle is 90° or 270°. Therefore the new current reference has to be limited to the magnitude of which ever component that has the lowest current rating. The current reference then becomes as shown in figure 5.3.

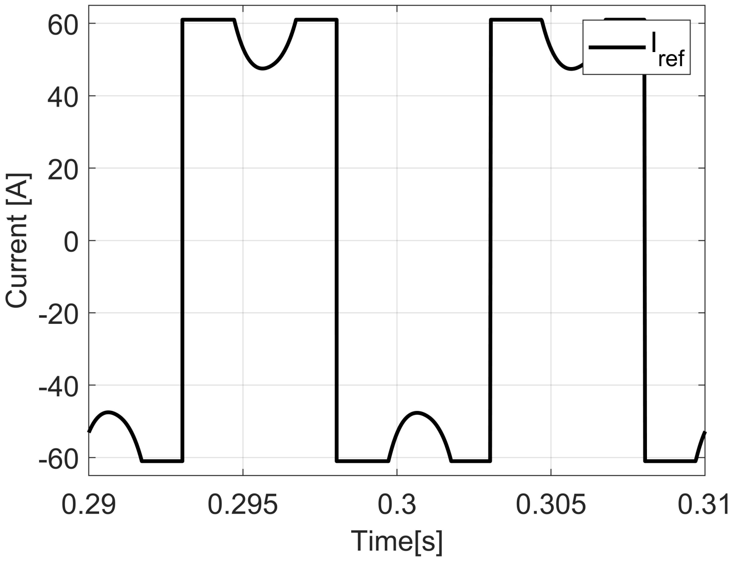

Figure 5.3: Method 1 open-phase control method current reference.

The current limit, shaping the current at the maximum and minimum values in figure 5.3, causes the machine to generate less torque than its reference value. Hence, as it is stated in [50], at low loads when the current magnitude is less limited, the average electromagnetic torque matches the reference well. But at higher loads the output is getting de-rated due to the increased current saturation.

Ideally the current should change polarity instantly, as it can be seen from the reference in figure 5.3. However, due to the stator inductance, this is not the case. Instead the current commutating gradually, causing the actual polarity change to happen with a few electrical degrees delay. This delay in commutation causes a negative torque production, reducing the performance of the already faulty machine. In order to mitigate this problem the so called prefire of the switches is implemented. This alters the theoretical switching angles of 90° and 270° to an "earlier" value to allow for the current to commutate according to the reference. The required time in which an earlier commutation has to be implemented is calculated as

$$t_{pre} = \frac{2L_s i_s}{V_{DC}} \tag{5.8}$$

from article [51] by the same authors as [50], both in which the method is thoroughly explained.

Method 2 -Per phase controller

The second control method implemented to handle open-phase faults, is an in-house developed control algorithm at Aros Electronics. The method decomposes every phase into two quantities, representing the magnitude and phase of the signal respectively, then controlling both quantities individually.

A sinusoidal current reference is required for the error signal calculation. The current magnitude is calculated from the average torque over one period, expressed as

$$T_{avg} = \frac{1}{2\pi} \int_0^{2\pi} i_s \psi_{pm} \sin^2(\theta) d\theta \tag{5.9}$$

which is then multiplied with a sin-function of the rotor angle as

$$i_{ref} = \frac{2T_{avg}}{\psi_{pm} n_p} \sin(\theta_{elec} + \phi) \tag{5.10}$$

where ϕ is the angle added in order to orient the vector in the corresponding direction of the voltage vector of which ever fault that has occurred. For phase A, ϕ is for example set to 90° in order to create the V_{BC} vector in figure 5.4.

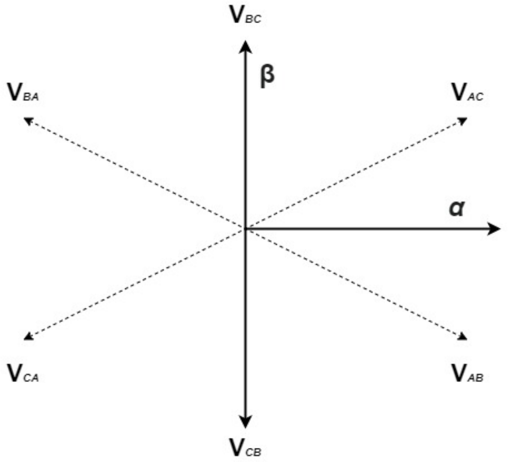

Figure 5.4: Voltage vectors.

Analogous to how the electrical angle θ is used as transformation angle in the dq transformation, θ is here used to transform the current error into DC values in order to be able to implement PI controllers, as shown in figure 5.5. The Sine transformation is chosen so that the D component controls the phase, and thereby the currents zero crossing. Much to the same effect as in control method 1, resulting in a reduction of the negative torque production. The Cosine function is then chosen to transform the Q component controlling the amplitude.

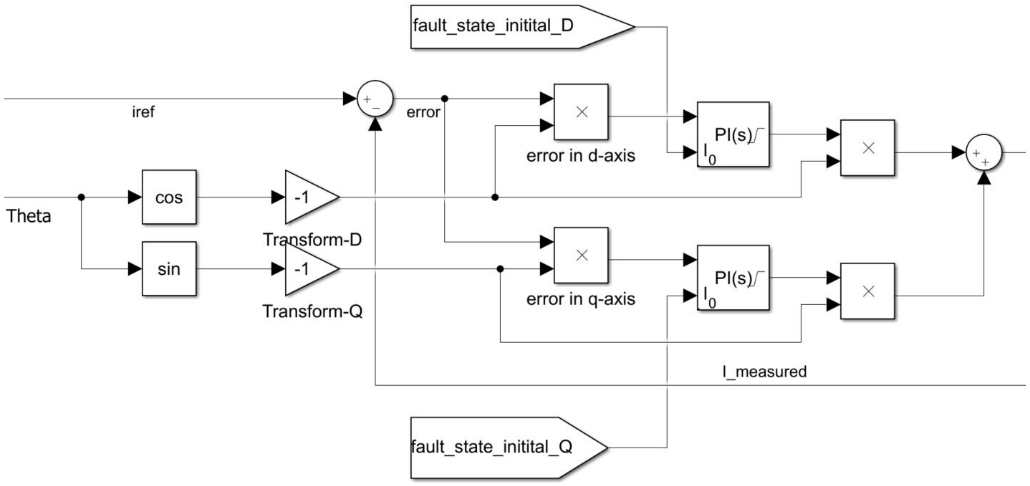
fault_state_initital_D
iref
error
error in d-axis
PI(s)
I0
Theta
cos
sin
-1
Transform-D
-1
Transform-Q
error in q-axis
PI(s)
I0
I_measured
fault_state_initital_Q

Figure 5.5: Per-phase controller Simulink implementation.

After the PI controllers the same trigonometric functions with a 90° phase shift are used to transform the quantities back into to AC values, where they are then summed together to one signal. Finally the voltage signal is then transformed into $\alpha\beta$ frame quantities as shown in figure 5.6.

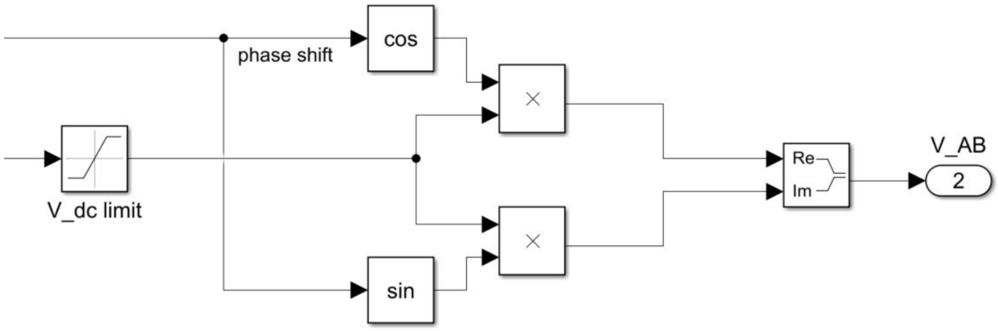
phase shift
cos
sin
V_dc limit
Re
Im
V_AB
2

Figure 5.6: Per-phase controller transformation.

The PI controllers use the same gains as the controller for the healthy operation and a current limiter is implemented after the current reference calculation. The inputs to the integrator blocks in the healthy operation controller are used as initial conditions for the integrator blocks in the fault-mode controllers to reduce transient behaviours, as can be seen in figure 5.5.

5.3.3 Resonant controller

The resonant controllers in [22] and [21] aims to reduce post-fault torque and speed ripple, thus increasing the post-fault performance. They also have the ability to reduce possible harmonics during healthy conditions. Therefore the resonant controller proposed in [22] and [21] is implemented in order to investigate its impact on the performance both pre- and post-fault.

The ideal resonant controllers has the transfer function

$$G_{c_{res}} = \frac{K_r s}{s^2 + (n\omega_e)^2} \tag{5.11}$$

where K_r is the controller gain, ω_e the fundamental electric frequency and n the harmonic order of interest [21]. Due to its narrow bandwidth and infinite gain, implementing the ideal resonant controller can lead to stability problems [52]. Therefore a quasi-resonant controller is used with the transfer function

$$G_{c_{res}} = \frac{K_r s}{s^2 + 2\omega_c s + (n\omega_e)^2} \tag{5.12}$$

where the ω_c is the cut off frequency of the controller. Including the ω_c gives the possibility to increase the bandwidth of the controller, thus increasing the controllers frequency robustness [21].

Figure 5.7 and 5.8 show the bode plot transfer function for the quasi-resonant controller at 1000rpm and n chosen to be the 6th harmonic. K_r is fixed to 200 in 5.7 while ω_c is varied. In 5.8 the opposite is done where ω_c is set to 10 and K_r is varied. The figure shows that peak gain increases with larger K_r but at a fixed bandwidth while ω_c both affects peak gain and bandwidth. The high open loop gain at at specified frequencies makes it possible for the controller to attenuate the selected harmonics.

It is evident that K_r and ω_c are important parameters for the performance of the controller. By basing the parameter values on what is used in [21] and adjusting them at different speeds and loads by trail and error, the values of $K_r = 200$ and $\omega_c = 10$ are used. As [53] states, a straight forward tuning approach for resonant controllers is barely available and a trial and error approach is often used. Since tuning them thoroughly requires a thorough analysis of the dynamic behaviour of the machine, it falls somewhat outside of the scope of this thesis as steady state values are the main focus. Instead the parameter gains have been set rather restrictively, and tested over a wide speed and load range of the motor, not to jeopardise the stability of the system.

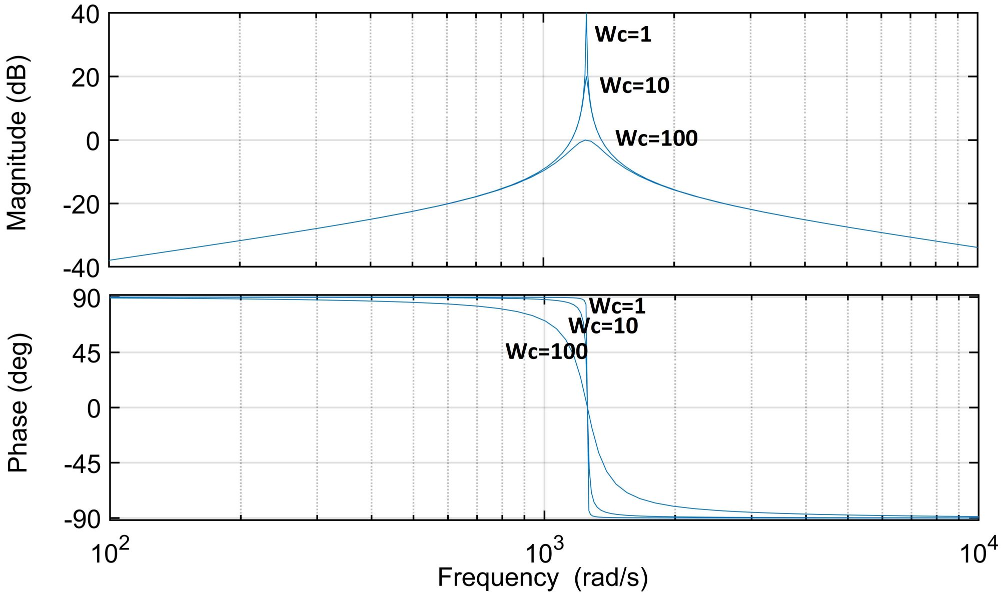

Figure 5.7: $\omega_c = 1, 10, 100, K_r = 200$.

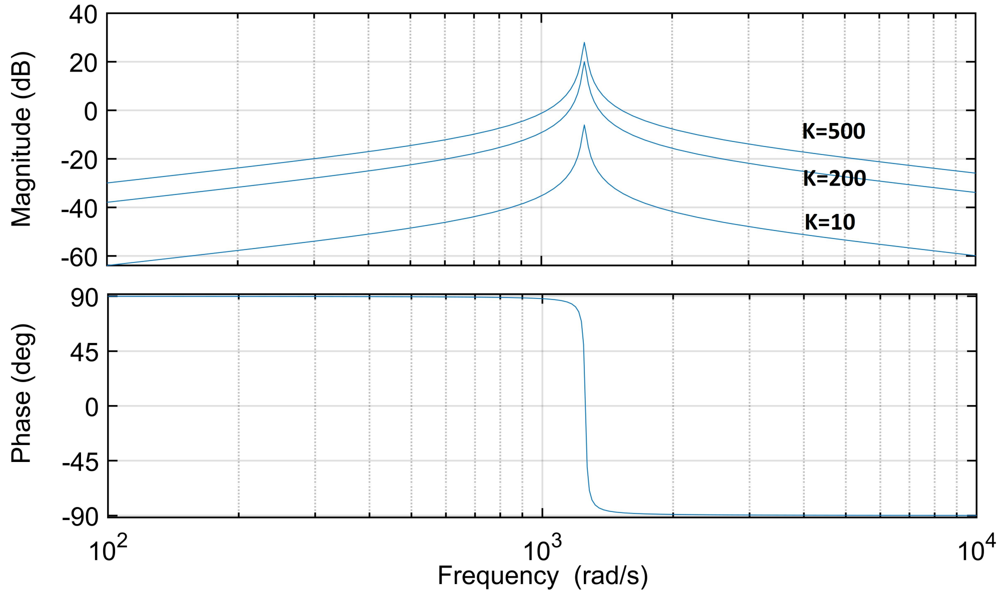

Figure 5.8: $\mathrm{K}_r = 10, 200, 500, \omega_c = 10$.

As is suggested in [34], the fundamental electric frequency, ω_c is fed through a low-pass filter and into the resonant controller in order to make it adaptable to its entire speed range. As seen in figure 5.9, several resonance controllers can be put in parallel with the standard PI-controller in the dq frame.

Figure 5.10 shows the implementation of (5.12) in Simulink with all its parameters. The n value, specifying what harmonic order the controller is operating on, is squared in the Matlab code in order to satisfy (5.12). The derivation of the expression for the Simulink implementation is provided in appendix B.

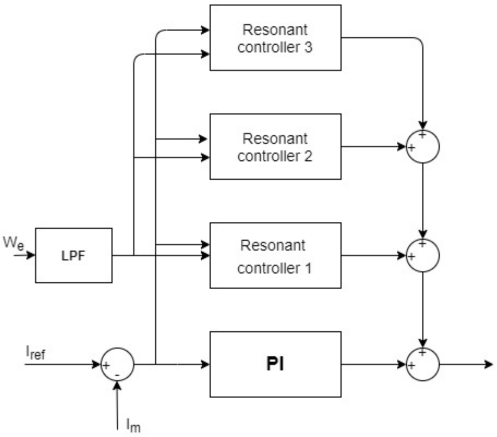
Resonant controller 3
Resonant controller 2
Resonant controller 1
PI
LPF
We
Iref
Im
+
-

Figure 5.9: PI controller with adaptive resonance controller.

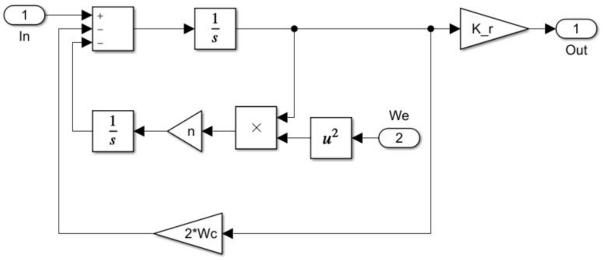
1
In
1/s
K_r
1
Out
1/s
n
×
u²
We
2
2*Wc
+
-
-

Figure 5.10: Resonance controller Simulink implementation.

The resulting bode plot of of the three parallel connected controllers is show in figure 5.11 where the gain at the three resonance frequencies 6, 12 and 18 can be seen. As mentioned, more parallel elements could be added if desired.

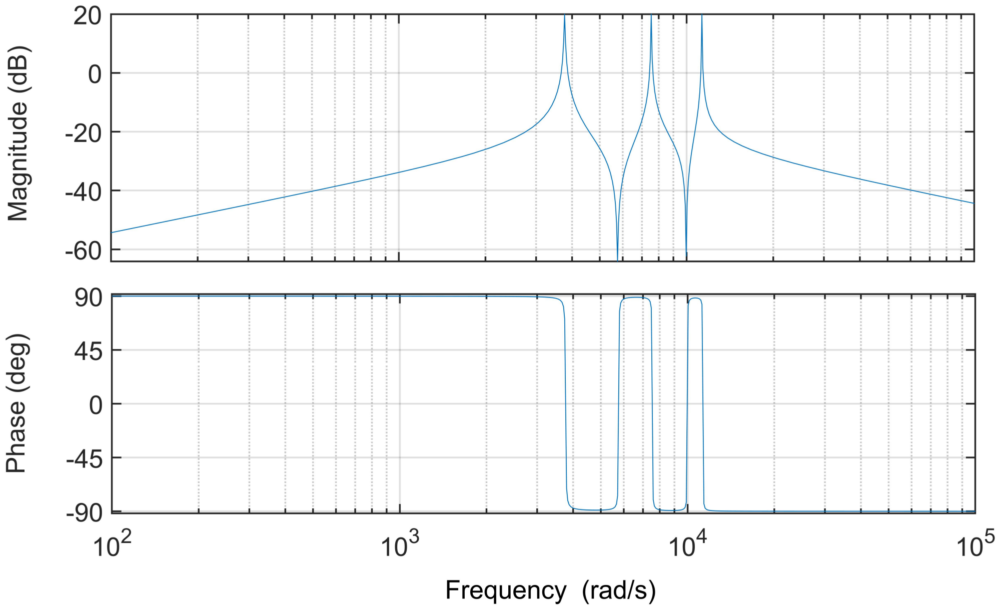

Figure 5.11: Bode plot transfer function for resonance controller with 6th, 12th and 18th harmonics chosen, K_r=200, ω_c=10.

6

Results and analysis

This chapter describes the different practical tests performed in the lab and the simulated cases. Measured values from the lab are compared against the simulated results in order to verify the model behaviour.

6.1 Performed tests and simulations

The studied machine is rated to produce 9.5Nm at 2800rpm, when it is connected as a single three phase machine. This rating is maintained when the winding is connected as two 3-phase sets with a maximum allowed RMS current per phase of 61A, as described in chapter 4.

The bench set-up described in section 4.3 is used for measurements. The load motor visible in figure 4.4 is set to the desired speed and the i_d and i_q currents are applied to the prototype machine with the same angle as calculated for MTPA in the simulations. Values for RMS current and average torque are measured alongside DC voltage and current.

No changes to the controller are made when testing the healthy operation or the three phase open cases. The position of the rotor is obtained with an encoder and the information is shared with both inverters through opto-isolated communication.

The bandwidth of the speed and current controllers are in the simulation model initially set to 200 and 2000rads/s respectively. All values presented are measured or simulated at steady-state conditions unless otherwise stated. For all cases where both lab-tests and simulations are performed the lowest and highest comparable operating points are compared. In order to have a comparable mid range operating point as well, the 40A rms point is arbitrarily chosen.

6.1.1 Healthy Operation of the dual winding machine

The healthy dual connected machine is tested at 500, 1500 and 2500rpm. The *dq*-current set points, obtained from simulations when sweeping the torque from 1Nm to the nominal torque output of 9.5Nm, are used as inputs to the test-bench. The simulation results are shown with the experimental results in figure 6.1 together with the torque-constant, $K_t = T_{nom}/I_{rated}$ representing the theoretical performance of the machine at rated current.

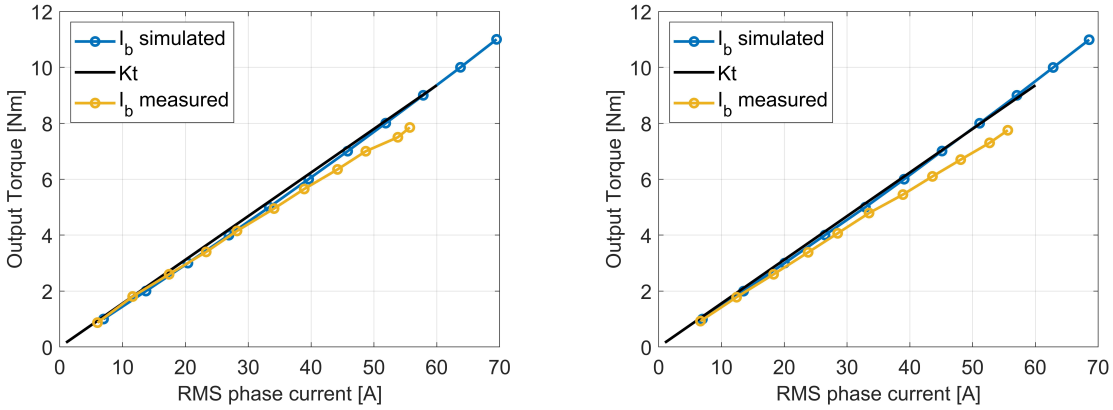

(a) 500 rpm (b) 1500 rpm

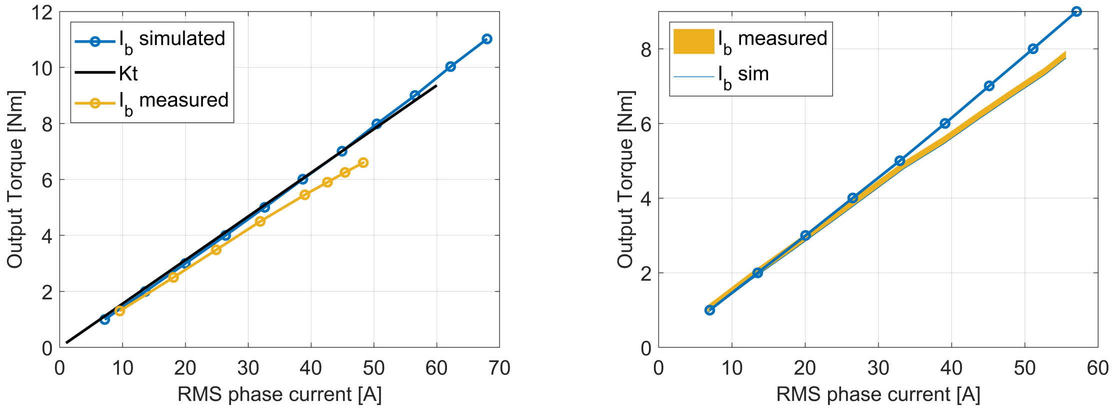

(c) 2500 rpm (d) Minimum measurement error

Figure 6.1: Simulations and Lab-test result for the healthy dual winding machine.

Overall the simulated values align well with the theoretical design values of the torque constant. The simulated values corresponds closely with the experimental results at low range while the deviation increases as the load and speed becomes higher at higher operation points.

One source of discrepancy between the simulation and the experimental values can be attributed to the measurement uncertainty originating from the characteristic tolerance of the transducer used to measure the torque. The device, mentioned in table 4.4, can have an error of ±1Nm at zero torque and ±0.1Nm at its rated torque, 50Nm. The minimum measurement error is therefore 0.1Nm and is shown as the thick line in figure 6.1d.

It can be noted that for the 500rpm case the model underestimates the torque output slightly for operating points below 20A rms, while overestimating it when above 20A rms. This however falls within the measurement error margin discussed in previous paragraph. The discrepancy in percentage between the measured and simulated values are shown in table 6.1 where the tendency of larger errors with both increased loads and speeds are visible.

The lower T/I_{rms}-ratio of the measurements at higher loads and speeds can be explained by magnetic saturation in the motor which the simulation model does not account for. At higher currents, for example, L_q is slightly decreased due to saturation. If this is taken into consideration for the MTPA angle calculation, the theoretically determined high power machine performance might behave more close to its measured characteristic.

Table 6.1: RMS current and difference in torque output

	Healthy dual winding operation					
	low range		mid range		high range	
	I_{rms}	$\%_{diff}$	I_{rms}	$\%_{diff}$	I_{rms}	$\%_{diff}$
500rpm	7	3.08	40	4.54	55	10.23
1500rpm	7	2.55	40	9.82	55	13.07
2500rpm	10	5.42	40	11.29	48	14.58

6.1.2 Three-Phase Open Circuit

It is possible that an inverter fails in such a way that the best way to continue operation is to completely disconnect it from the motor. A similar case could occur if the inverters are fed from separate DC-sources and one source fails. Similar tests are therefore performed as the previous test cases at 1500rpm with only one inverter supplying one of the windings. The same scenario is simulated in Simulink by introducing the faults as explained in section 5.2. The results are shown in figure 6.2. In this case, K_t is calculated with $T_{nom} = 4.75$Nm.

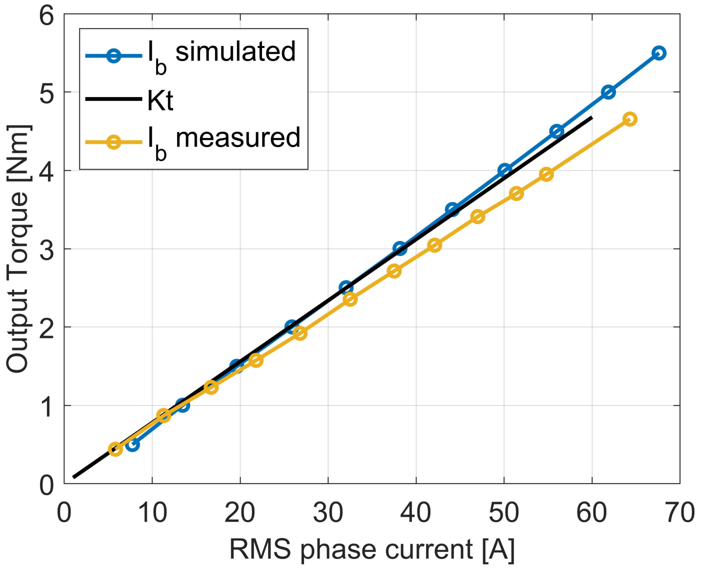

Figure 6.2: 1500rpm, 3 phase open.

As figure 6.2 shows, when operating the machine on only one winding, 4.4Nm of torque are produced at the nominal rms current of 61A. As the K_t line shows, the theoretical value is half of that of nominal load at 4.75Nm. The simulation slightly overshoots the K_t value but the high range discrepancy between simulation and measurements are of the same order as for the healthy case, as shown in table 6.2.

Table 6.2: RMS current and difference in torque output

	Three phase open operation					
	low range		mid range		high range	
	I_{rms}	$\%_{diff}$	I_{rms}	$\%_{diff}$	I_{rms}	$\%_{diff}$
1500rpm	8	14.56	40	9.34	61	11.56

The high error in the low range operation point in table 6.2 is likely due to measurement error as discussed earlier. Due to the slightly different gradients of the simulated and measured values that can be seen in figure 6.2, the lines overlap at 14A rms. Consequently, the error is 0% at this point, with a relationship between the measured and simulated values analogous to earlier tests in section 6.1.1, at higher loads.

A simulation is run at the 1.5Nm load since the T/I_{rms}-ratio closely matches between simulated and measured values in this range. A slight unbalance in the *abc*-currents can been seen in figure 6.3, which can be attributed to the non ideal inductances and back emf, which is in line with the findings in [16] and [21].

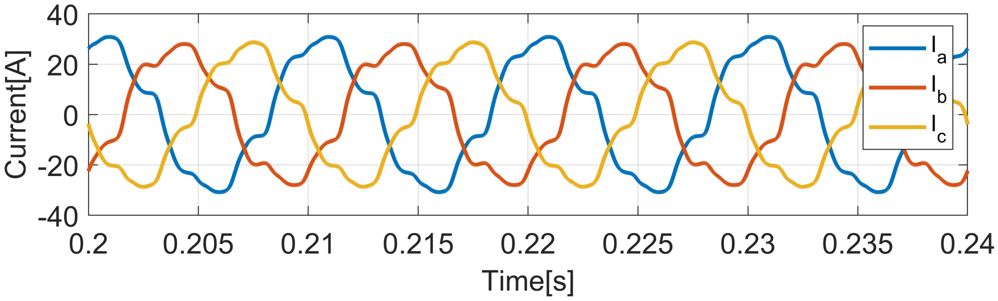

Figure 6.3: 1500rpm, 3-phase open phase currents of winding B at 1.5Nm load.

6.1.3 Comparison of tests

Figure 6.4 shows the measured results for the dual winding healthy operation (DH) and the three phase open circuit (3PO) case at 1500rpm for one winding, on the same plot. The behaviour is as expected at the for the 4Nm operating point, where the DH-case requires 28A rms per phase while 3PO requires almost twice the amount (55.6A). However, for higher operating points, the DH machine produces 7.75Nm at 55.6A, while the 3PO produced 4Nm at the same current. The expectation is that the DH machine could produce twice the torque as the 3PO case, if both cases have the same current per phase. The lower result could be due to the simultaneous operation of the windings, where an increased saturation of the stator is likely since close to rated current is flowing in all phases. Coupling between the windings could also be a factor, since the separate control implementation does compensate it.

It is worthy to note that joule losses for the 3PO case will be twice as large as DH case for the same torque, assuming exact doubling of the phase current after the fault. The relationship is only 2x and not 4x since there are twice as many phases in the DH case.

The torque-per-ampere ratio in the DH case is close to exactly double the ratio in the 3PO case, meaning that the “effectiveness” of the current to produce torque is reduced by half, as expected. However, since there are more losses, this configuration is also less efficient.

Figure 6.5 shows the losses for the DH and 3PO case, at 1500rpm, calculated from the difference between the measured input power and the mechanical power at the shaft. The plot shows higher losses for the 3PO case than the DH case, except at low torque. This can be due to increased measurement errors at low power, both for the input power and torque.

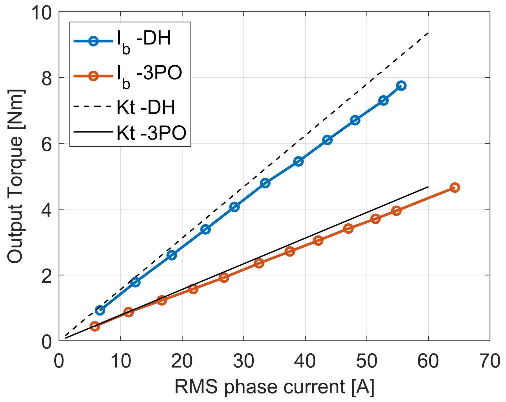

Figure 6.4: Measured results for DH and 3PO cases at 1500rpm.

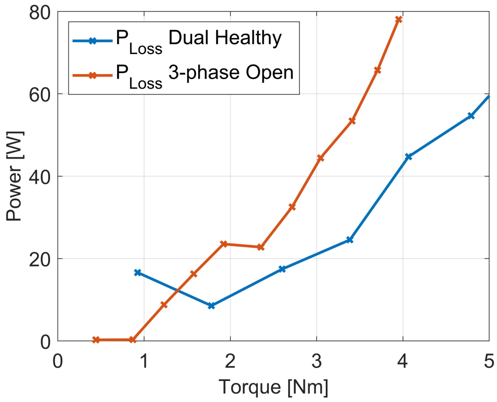

Figure 6.5: Losses for DH and 3PO cases.

6.2 Single-Phase Open Circuit

In this scenario, the torque production capabilities of a single winding is tested while it undergoes a single phase open fault. Although magnetic coupling is limited between the windings, the other winding is disconnected in this case to avoid any coupling interaction and more accurately quantify the single winding's capability and torque contribution.

6.2.1 Lab verified open phase cases

Two versions of this case are tested in the lab, both conducted at 1500rpm. First, a test with one phase-open with no post-fault control implemented is performed, to compare against the post-fault control strategy. The inputs are, as in the healthy case, the i_d and i_q currents calculated for different loads. Secondly, the per-phase controller introduced in section 5.3.2 is implemented and tested. In this case, the input is the current magnitude for the post-fault controller as calculated by (5.10). The same cases are again recreated in Simulink with the faults implemented as described in section 5.2. The measured values are shown in figure 6.6 and 6.7, along with the simulated values.

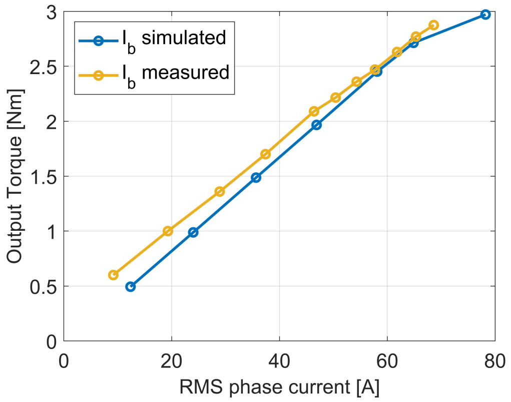

Figure 6.6: One winding with one phase open, *dq*-controller -lab vs sim.

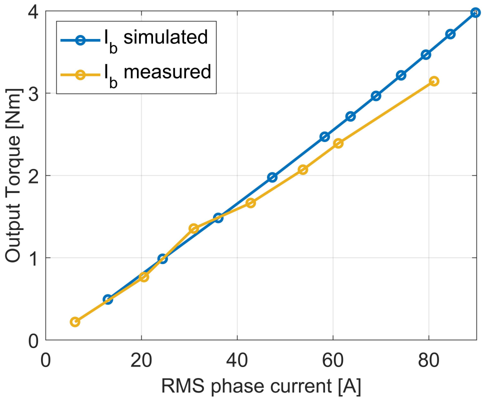

Figure 6.7: One winding with one phase open, per-ph controller-lab vs sim.

As can be seen in figure 6.6, the torque output has in this case decreased to 2.64Nm at rated rms current. Which can be compared with the 4.4Nm observed in the previous test shown in figure 6.2, giving a ∼41% reduction of output torque when loosing one phase. A very similar result can be seen for the per-phase controller in figure 6.7.

It should be noted that, for the case shown in figure 6.6, contrary to the earlier cases the model now underestimates the torque output. The characteristics of the error is also reversed compared to previous cases with a larger discrepancy at low range operation points. However, for the operation point at rated current, the simulation is very close to the measured value, as shown in table 6.3. The deviations can, as for the earlier cases, possibly originate from measurement errors. That the slope of the measured values in figure 6.7 do not extrapolate downwards to the origin, as in all other cases, might indicate that the measured values are slightly too high for low range operation points.

The results from the per-phase controller test and simulation, seen in figure 6.7, shows very similar behaviour to earlier tests. The non-linear behaviour of the measured values around 30A rms is most probably due to measurement error. The differences between measured and simulated values, shown in table 6.3, are for this test the smallest of all performed tests for both low, mid and high range operation points. The percentage value at the 40A rms point is however slightly distorted due to the measured value at this point. If the difference instead is calculated at 43A rms, it becomes 6.4%.

Table 6.3: RMS current and difference in torque output at 1500rpm

Open phase operation, no post-fault controller and per-phase controller						
	low range		mid range		high range	
	I_{rms}	$\%_{diff}$	I_{rms}	$\%_{diff}$	I_{rms}	$\%_{diff}$
dq-controll	12.3	31.9	40	7.7	61	1.3
Per-phase	13	2	40	4.1	61	8.8

Figure 6.8 shows the measured and simulated torque at 1500rpm when a load step of 2Nm is applied. The average of both output signals are 2Nm. The measured signal is the mechanical torque and is thereby filtered through the mechanical system while the simulated signal is the electromagnetic torque. The discrepancy in amplitude is therefore expected. The machine performs remarkably well during one-phase open conditions when no post-fault controller is implemented. There is only a slight negative electromagnetic torque production of less than 0.1Nm in the simulations. When the per-phase controller is applied this is however reduced to zero after the controller has settled at steady state conditions, as can be seen in figure 6.9.

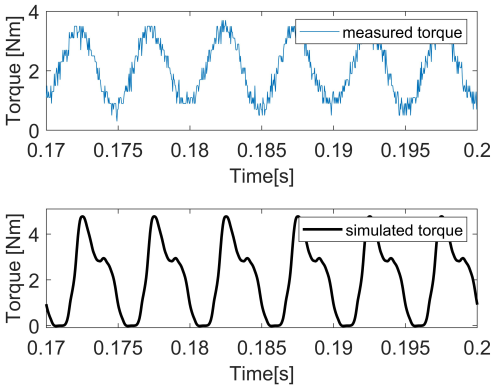

Figure 6.8: Open-phase *dq*-controller, measured and simulated torque ripple at 1500rpm, 2Nm.

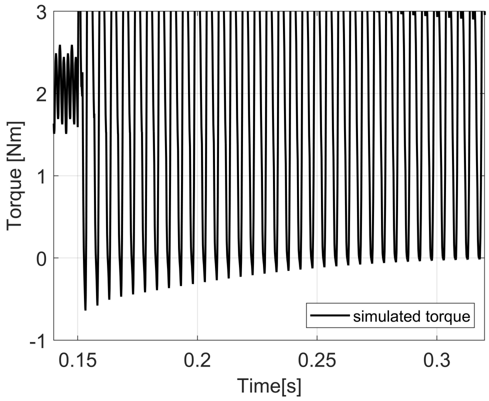

Figure 6.9: Per-ph controller, controlling away the negative torque at 1500rpm, 2Nm.

Figure 6.10 shows a comparison between the 3PO case and the single phase open circuit cases. As seen, the torque-per-ampere is further diminished; more current is needed to produce the same torque. Figure 6.11 is similar to 6.5 and shows losses for the single phase open fault case, with the normal dq controller, are larger for a given output torque, indicating reduced efficiency.

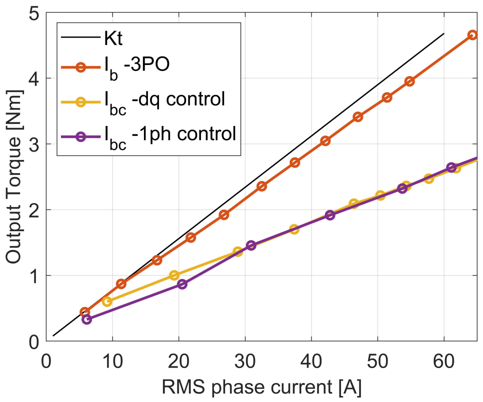

Figure 6.10: Results for 3PO and 1ph-Open case, with per-phase control and with dq control.

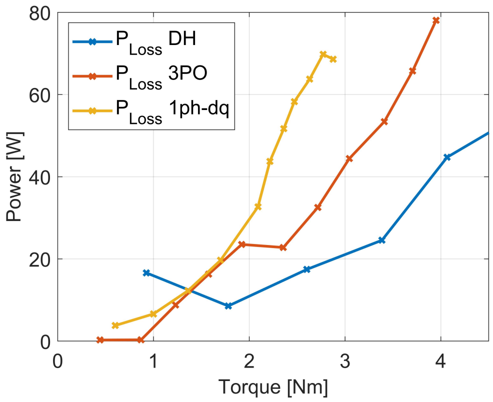

Figure 6.11: Losses of DH, 3PO and 1ph-dq cases.

6.2.2 Simulated open phase cases

The post-fault pre-fire method introduced in section 5.3.2 is not validated through lab-tests, however it is implemented in the model and simulated at 1500rpm for comparisons sake.

The simulated results from said method are very dependant on current-limits and bandwidth of the current controller. As discussed in section 5.3.2, the current limit is the deciding factor for the maximum current amplitude. Hence, if the current limit is chosen to a magnitude of 61A, at high loads the current will theoretically become completely square and result in a 61A rms current. The theoretically instant current commutation also requires the controller to be very fast in order for the output current to follow the reference current. At lower current controller bandwidths the waveform become more and more distorted, therefore altering the rms-value.

To show the functionality and capabilities of the control method, a simulation where α_c = 10000rads/s at 1.8Nm load is shown in figure 6.12. At the end of the first I_{ref} period it can be seen how the I_{out} starts to commutate when the reference switches polarity. The time it takes for the current to drop to zero causes a slight negative torque production. The pre-fire algorithm is therefore engaged at 0.3s and the new current reference is shown as the dashed line. At the two following instances of commutation, the earlier switching action results in that the current changes polarity at the angles 90° and 270° instead of lagging behind and the negative torque is removed. A simulation at higher load is shown in figure 6.13 in order to exaggerate the effect which is not clearly visible in figure 6.12. The two first cycles shows the negative torque, and the following two cycles shows how it disappears when the pre-firing is activated.

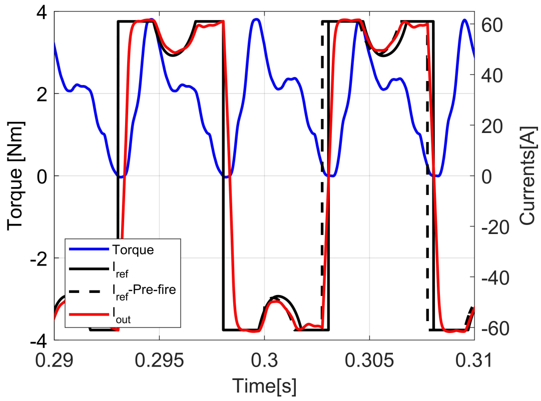

Figure 6.12: Current reference with and without prefire, torque and commutating current.

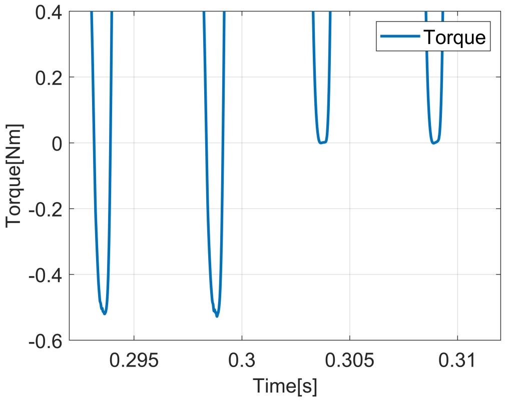

Figure 6.13: Negative torque with and without pre-fire during post-fault operation.

Since the maximum torque production is desired close to 90° and 270°, a current limit of 61A is not optimal. To allow for the $1/\cos(\theta)$ shape of the current from (5.7), in order to maximize the current and consequently the torque production closer to the switching instances, a higher current limit performs better. The 61A current limit is therefor multiplied by two for the nominal current case shown in table 6.4 and multiplied by three for the maximum operation point.

L_s in (5.8), used to calculate the pre-fire angle, is approximated to L_q and i_s is set to the current limit. In order to perform a fair comparison with the other control methods, i_s should be continuously updated and the current limit should be optimised to reduce the rms value for every load level. Since the result is not experimentally validated this is however not done. In table 6.4 the pre-fire operation points are for comparison sake simulated at 2000rad/s giving it a more favourable rms current. The T/I_{rms}-ratio is however nonetheless worse than for the two other cases.

Although the pre-fire method performs less favourable when comparing T/I_{rms}-ratios, it can push the performance up to the max rms current and produces the highest torque output at 4.9Nm as seen in table 6.4. The drawbacks of not having the possibility of starting once stopped, as noted in [50], is for the dual layout analysed not an issue since the healthy winding can be used to perfome this task. The max operation point shown table 6.4 is also simulated with current controller bandwidth of 10000rads/s with a similar result.

6.2.3 Single-Phase Open summary

Table 6.4: Performance comparison for the different one- phase open cases

Performance of post-fault control strategies				
Nominal current		Max operating point		
Case	T_{load}	$I_{rms_{nom}}$	$T_{load_{max}}$	$I_{rms_{max}}$
No controller	2.65 Nm	61.7 A	3 Nm	78.2 A
Per phase controller	2.69 Nm	61.8 A	4.2 Nm	101 A
Pre-fire controller	2.3 Nm	61.9 A	4.9 Nm	134.6 A

As the comparison in table 6.4 and the plotted values in figures 6.6 and 6.7 suggest, performing no action and implementing the per-phase controller in post-fault conditions have marginal effects for low range operating points. However, when loading the machine more, the per-phase controller performs better. The max operation point in table 6.4 for the no-controller case is the last load-step before the simulation can not keep the speed reference anymore. The per-phase controller can actually keep the speed reference at loads above 5Nm, but with a very long settling time and high transient currents. Therefore a current limit of 3 times 61A was chosen for this operating point to keep the transient behaviour within reasonable values.

It can be concluded that the pre-fire controller needs a very fast current controller and has a poor T/I_{rms}-ratio at low operating points. It however have a very high load operating capability under faulty conditions and very stable transient behaviour. If high torque capabilities under intermittent load cycles is the requirement, it can be a good choice.

The per-phase controller has a longer settling time when a fault occurs and the transient behaviour can be an issue. When comparing the T/I_{rms}-ratio, the method however outperforms both other approaches over a reasonably wide operational range in post-fault conditions. It can therefore be a good choice if a continuous operation is the most important requirement even after a fault occurs.

6.3 Balanced Short circuit

Calculations from (3.1) and (3.3) are performed with parameters from table 4.1 for the dual-winding connected machine, and the value of ψ_{pm} from table 4.2 was reduced by 10%, as mentioned in previous sections, due to the skewing of the rotor. The results are plotted in figure 6.14 along with measurements of a balanced short circuit on one of the windings, while the other is disconnected. The figure shows that the maximum amplitude of the short circuit current at rated speed approaches 270A, as indicated by $I = \psi/L_d$, discussed in section 3.1.1, which would damage the healthy winding.

Measurements coincide well with calculation of the current, and show that if a three phase short circuit were to occur, the amplitude of the current induced in the affected winding would become 85A at 145rpm. Furthermore, measurements differ from the calculations for the breaking torque for an unknown reason. Nevertheless, the maximum measured breaking torque becomes -6Nm at 400rpm and therefore the unaffected winding would experience a severe increase of load, exceeding its rated capability. From this analysis, it is clear that operation under a three phase short circuit is very limited and can result in severe damage to the windings. The balanced short circuit fault could not be simulated accurately with the model built in Matlab.

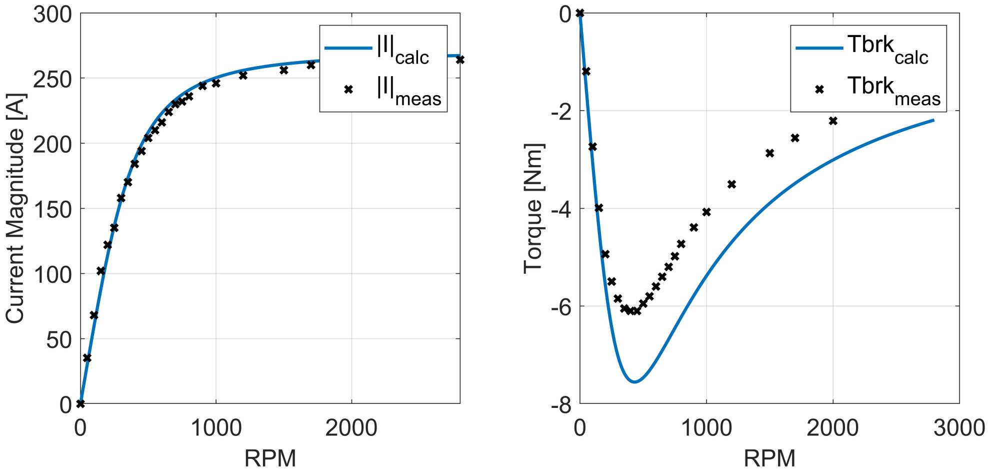

Figure 6.14: Behaviour of current and torque during a three phase short circuit.

6.4 Additional performed tests

In order to verify the reliability of the measured results, some of the experiments where repeated. However, these additional measurements did not reproduce the same results. The reason, at the moment of writing this thesis, is unknown. A repetition of all measurements is proposed, in order to increase the confidence of the results and hence prove or disprove repeatibility of the experiments.

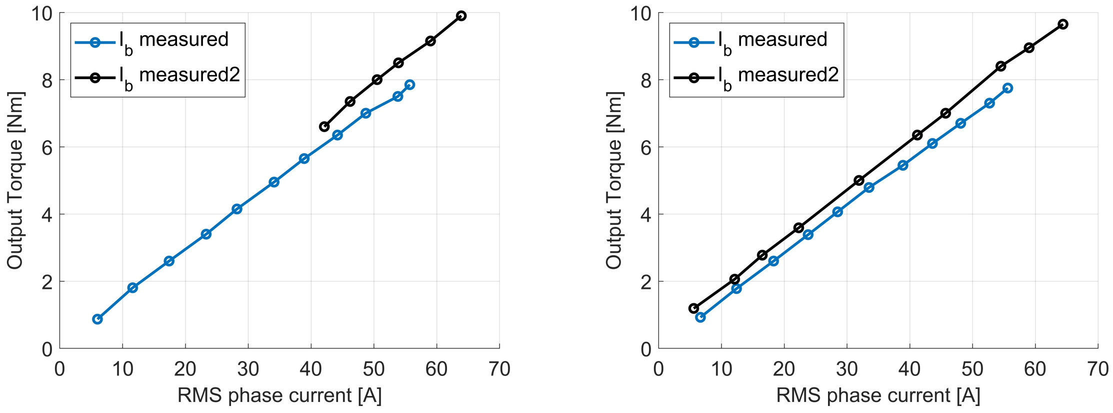

(a) 500 rpm (b) 1500 rpm

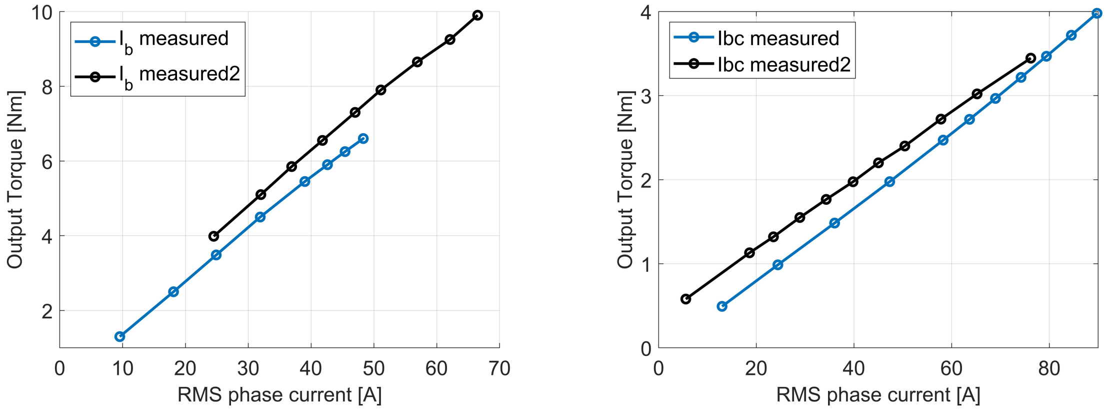

(c) 2500 rpm (d) 1-ph controller

Figure 6.15: First and second round of experimental tests.

6.5 Resonance controller simulations

The resonance controller introduced in section 5.3.3 is implemented and its effect is first investigated on the healthy dual machine performance, then the various faulty cases. There are two main differences between the cases investigated in [21] and [22], where resonant controllers are used, and the machine analysed in this thesis. The first case is a dual-winding layout with a neutral wire present between the Y-points and the second case is a standard three-phase machine with a neutral connection to the inverter.

6.5.1 Healthy dual operation

The healthy dual machine is simulated at 500, 1500 and 2500rpm with and without the resonance controller engaged at a 3Nm load to investigate its performance at different speeds. 3Nm load is chosen since at this load the model closely resembles the measured values, as figure 6.1 shows, where the load is shared equally between the winding sets. A fast fourier transform(FFT) analysis is performed with the Powergui tool in Simulink. The results are shown in table 6.5.

Table 6.5: Healthy dual operation at 3Nm load

Total harmonic distortion(THD) at different speeds		
	No resonant controller	With resonant controller
rpm	THD	THD
500	11.4 %	6.3 %
1500	12.6 %	2.4 %
2500	12.8 %	1.9 %

The resonance controllers are tuned as described in section 5.3.3 with, for this case, the 6th, 12th and 18th harmonics are chosen to be suppressed. This results in the suppression of the 5th and 7th *abc* current harmonics as shown in figure 6.16 and 6.17, where it can be noted that the 11th and 13th harmonics have totally disappeared in the latter case.

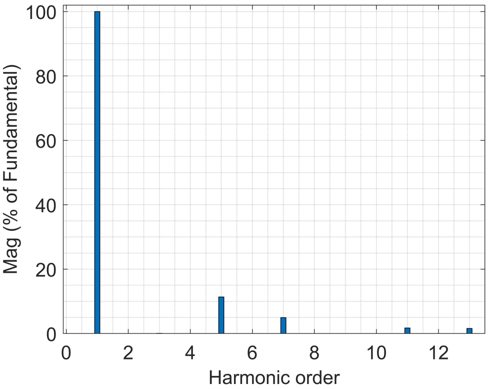

Figure 6.16: *abc*-current harmonic content with no resonant controller, 1500rpm, 3Nm.

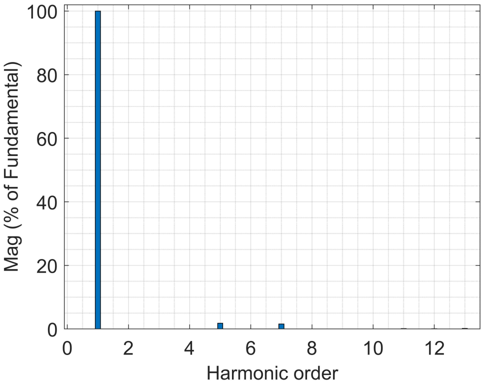

Figure 6.17: *abc*-current harmonic content with resonant controller engaged, 1500rpm, 3Nm.

The system is in this case balanced, as can be seen from the absence of 3rd order harmonics in 6.16. The results in table 6.5 and figures 6.16-6.18 are equal for all currents of both windings.

The effect on the current over four periods can be seen in figure 6.18.

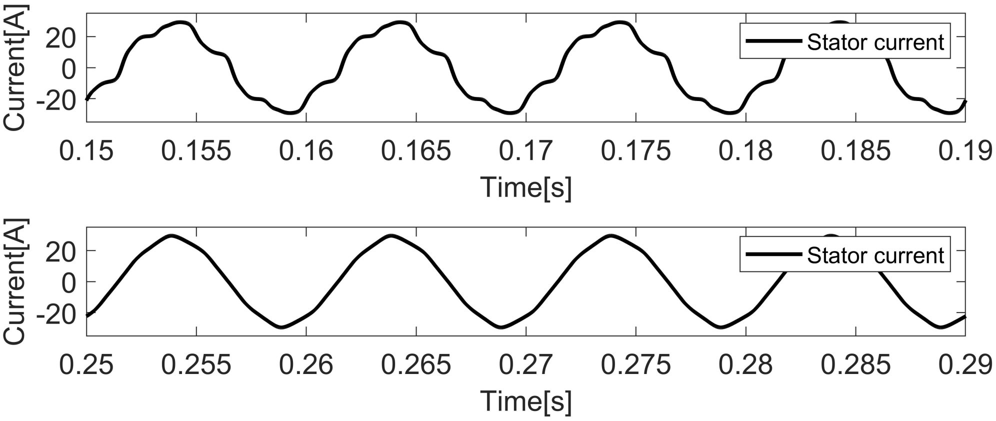

Figure 6.18: Stator current at 1500rpm, 3Nm load, with and without resonant controller.

The torque ripple is, as expected, reduced while the average torque remains the same when the *abc*-current harmonic content is reduced. Figure 6.19 shows how the ripple decrease from ±0.7Nm to ±0.5Nm at this specific load and speed when the resonance controllers are engaged.

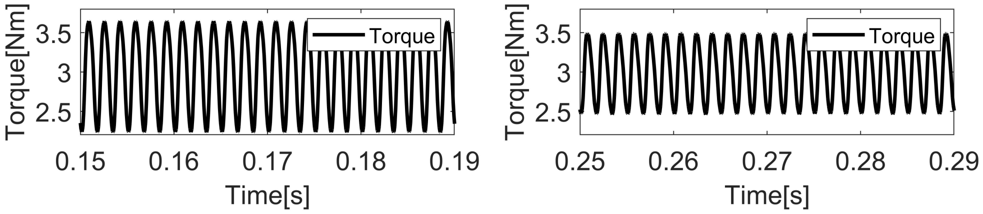

Figure 6.19: Torque at 1500rpm, 3Nm load, with and without resonant controller.

6.5.2 Three-phase open operation

The same simulation as in figure 6.3 is performed again and a FFT analyse is done on the *dq*-currents. As figure 6.20 shows, 2nd and 4th order harmonics are now present in the *q*-current with a THD of 10.6%. The harmonics are even higher in the *d*-current, at a THD of 86%, but as the main torque producer the *q*-current is the one shown. Consequently, an extra parallel resonance controller is implemented in the current controller and the 2nd, 4th, 6th and 12th harmonics are selected to be suppressed. The resulting *q*-current harmonics are shown in figure 6.21, now with a THD of 1.7%. The *d*-current THD is reduced to 6.5%.

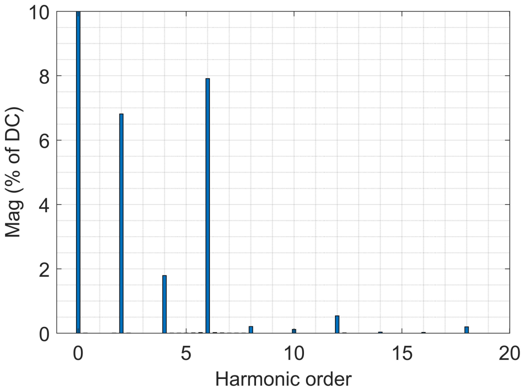

Figure 6.20: q-current harmonic content with no resonant controller, 1500rpm, 1.5Nm, 3-phase open.

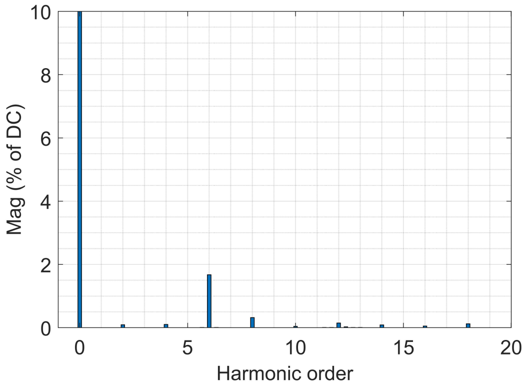

Figure 6.21: q-current harmonic content with resonant controller, 1500rpm, 1.5Nm, 3-phase open.

The corresponding *abc*-currents are shown in figure 6.22 where the resonant controllers are engaged at 0.35s. The THD of the currents prior to 0.35s is 11.7-14.3% and is then reduced to 1.3-1.7%. The torque ripple is reduced from ±0.45Nm to ±0.26Nm.

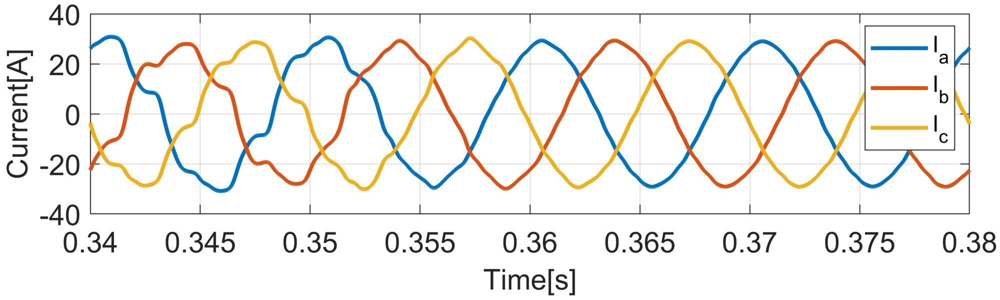

Figure 6.22: 1500rpm, 3-phase open, *abc*-currents of winding B at 1.5Nm load with resonant controllers applied at 0.35s.

As [22] states, the presence of the 2nd order harmonics in the system results in poor reference tracking for the PI-controller which operates on DC-values. The improved performance of the controller can be seen from observing the *dq*-current controller error-signal shown in figure 6.23.

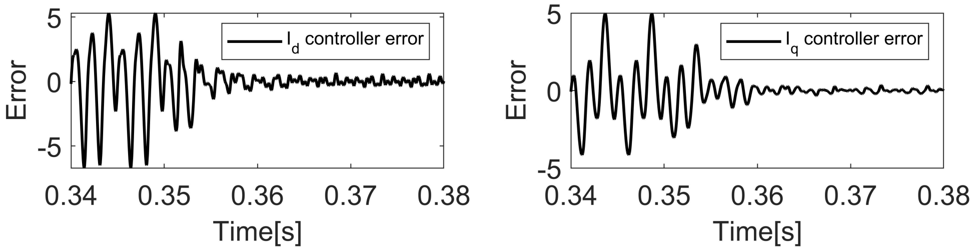

Figure 6.23: *dq*-current controller error signals, resonant controllers engaged at 0.35s.

6.5.3 Dual winding operation with one phase open

To investigate how an open-phase fault in winding B effects the operation when winding A is operating normally, simulations at 5Nm was performed with both windings sharing the load equally. At this low load, running the healthy winding at nominal operation and reducing the output of the faulty to as low as possible should be the most beneficial operating strategy, since this reduces the cross-coupling effects between the windings. The simulations are however performed this way in order to investigate the harmonic content in winding A when winding B suffers an open-phase fault. The 5Nm total load is chosen since at 2.5Nm load per winding, the model matches well with measured results, as seen in figure 6.2 and 6.6.

The FFT analyse in figure 6.24 shows a very prominent 2nd order harmonic with a THD of 26.7%. The same harmonics as in section 6.5.2 are chosen to be suppressed by the resonance controllers.

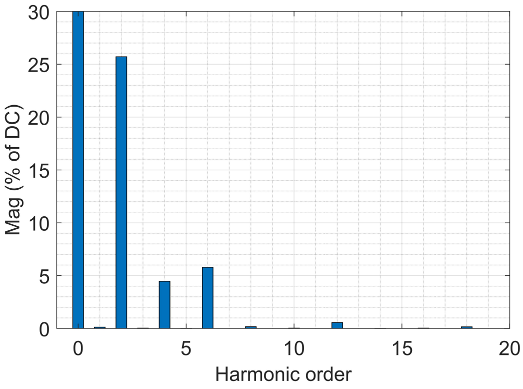

Figure 6.24: q-current harmonic content with no resonant controller, 1500rpm.

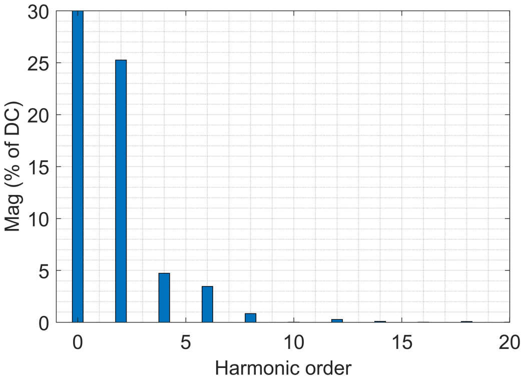

Figure 6.25: q-current harmonic content with resonant controller, 1500rpm.

As figure 6.25 shows, the resonance controllers can however not suppress the 2nd order harmonic induced from the faulty winding in this case. Only the higher order harmonics are suppressed which results in a THD of 25.9% and a slight torque ripple reduction.

The unbalanced currents in winding A, caused by the faulty B winding, is shown in figure 6.26

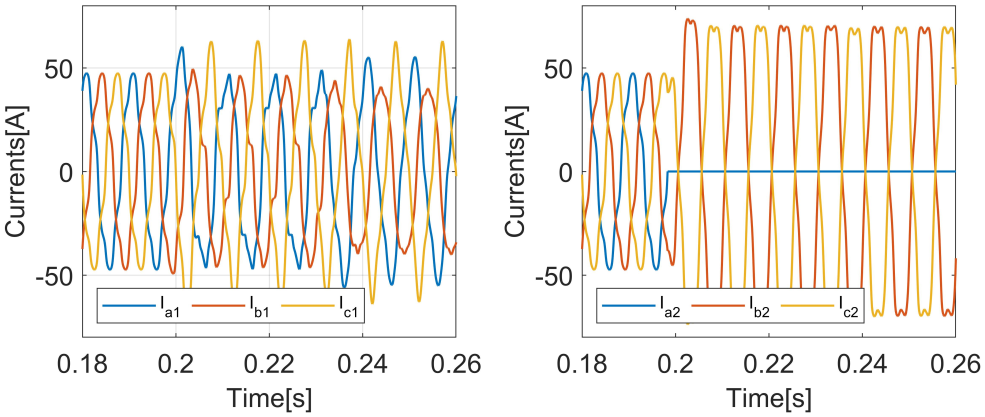

Figure 6.26: *abc*-current winding A and B, Open-phase in winding B at 0.2s, resonant controllers in winding A engaged at 0.23s.

The PI-controller current-error is in this case not able to be reduced because of the large disturbance from the faulty winding. It can therefore be concluded that the neutral connections used in [21] and [22] are needed in order to use the resonant controller as the actual post-fault controller.

6.6 Sustainability Aspects

The study of fault tolerance is especially relevant in the context of sustainability. There are two main aspects to consider when considering a comparison of a machine with extended reliability and one without special consideration to fault tolerance. The first of these is the potential to reduce the amount of material that is scrapped when a winding becomes damaged, and the second, is the extended productive time of the machine.

Regarding the first mentioned aspect, a modular approach to the winding can be valuable. This approach means that only the damaged part of the machine must be replaced, instead of the entire winding. This also implies less time spent in the re-manufacturing process, and hence less resources. Furthermore, a concentrated winding approach, where coils are wound around a single tooth, reduces the likelihood of a fault to occur between to coils, or phases, when compared with a distributed winding approach. With this approach the motor is less likely to need a winding replacement, thereby reducing wasted material and remanufacturing resources.

The second aspect is also benefited from the winding arrangements what where just mentioned. The modular winding approach implies that the healthy windings can still provide torque normally, provided there is no damage to their inverters, hence prolonging the time before maintenance must be performed. With a concentrated winding, the reduced fault probability will also prolong the productive time of the machine.

The benefits of this approach must be weighted against the increase in cost and additional materials used to produce the fault tolerant machine and drive. For this reason, this thesis is concerned with methods to retain post-fault capability of the drive with minimal investment. Applications where very robust reliability is needed might call for considerable investment and additional materials, however, this drawback can be balanced by the increased reliability itself. One example of this is in aircraft fuel pumps, as discussed in [25]. A failure of a motor in such situation would be catastrophic, and the costs of the failure will dramatically exceed any cost related to improvement of the drive.

7

Conclusion

Based on the findings from the previous chapter, the prototype machine described in chapter 4 has a reasonable inherent fault tolerance to open circuit faults. In case one of the windings or one of the inverters fails, the other can comfortably continue operation up to 50% nominal torque without any modification whatsoever. The remaining winding can also start the machine from zero speed, provided the initial rotor position is known.

Furthermore, the usefulness of the machine in a 3PO state is dependent on the application that it should be used for. In case of high load operation, an intermittent drive cycle is more favourable. The reason for this is that the winding can be operated above its nominal torque for brief periods of time, and therefore the only drawback is the increased losses in the system.

Section 6.2 presents the capabilities of one of the windings in case of a single-phase open circuit. If no change to the controller is implemented, the winding perform surprisingly well at low torque loads. At loads above 3Nm, a post-fault strategy is however essential to maintain a controlled output.

Two control strategies are evaluated and compared with the case where no post-fault control is implemented. The pre-fire method and the per-phase controller. The per-phase controller results in a very similar T/I_{rms}-characteristic to when no post-fault controller is implemented. It can however output much higher torque, with the limits being how high transient currents that are acceptable and how long settling time is allowed. The pre-fire method exhibits a lower T/I_{rms}-ratio but a very stable transient performance and high torque output capability. The very fast current controller needed might however prove problematic when implementing the method in practice. The findings, summarised in section 6.2.3, suggests the per-phase controller can be an option for continuous post-fault operation at lower torque loads, and the pre-fire method an option for intermittent high load cycles.

Both of these cases, 3PO and single phase open circuit, are less effective at producing torque within the machine. This is clear from the torque-per-ampere ratio, which indicates higher current magnitudes are necessary to produce the same torque, since less coils are available to produce said torque. This leads to a reduction in efficiency, since higher currents cause higher joule losses.

The implementation of a resonance controller is investigated in section 6.5. It is found that harmonic content and torque ripple is effectively reduced for healthy-dual as well as three phase-open operation. If the resonance-controller is to be used as post-fault controller in the case of open-phase faults, it is however found that a neutral connection between the windings Y-points is necessary.

Short circuit tolerance is practically nonexistent. In the case a short circuit occurs, this particular machine would not be able to produce torque with the healthy winding, due to the excessive breaking torque. If operation was forced, the currents induced in the shorted winding would be more than 4 times the rated continuous current.

The practical implementation of the above findings necessitates quick identification of the fault and the implementation of the post-fault control algorithm. Furthermore, as mentioned in the scope of this thesis, the affected leg, or legs, would need to be quickly isolated to prevent further damage to the inverter. In addition, in the case of a single-phase open circuit, a master controller should be implemented which could share the load between windings, taking into account their new, degraded, capability. An example of this would have the healthy winding operate the machine entirely on its own for loads lower than 50%, and have the other winding complement the torque production only if the load surpasses the 50% level for continuous operation. This would also reduce the torque ripple as well as the harmonic content in the healthy winding.

7.1 Future work

The results show modeling of the motor in this manner performed in this thesis provides results that match reality with reasonable accuracy. The method, however, always utilizes an inductance matrix obtained from only one operating point. Inductance, however, is dependent on the currents in the stator; large currents saturate the core. Therefore, the model can be improved by implementing an additional dimension to the lookup table used to obtain the inductance data where their dependence on current is accounted for. Furthermore, it could be interesting and useful to improve the model such that short circuit faults can be accurately simulated, including the breaking torque.

Regarding the control techniques, a method for a multi winding machine where the a decoupling of the windings is discussed in [54, 55]. This method was ignored due to the relatively low magnetic coupling between the windings in the segregated configuration. However, it is evident from these reports that oscillations in torque and speed can be minimized if this is accounted for.

The winding arrangement in the machine is such that connections to the individual coils are available. This indicates the possibility to connect each of the windings to a 6-leg inverter. This method would half the current rating for each of the inverter legs and could provide more reliable operation in case of an open phase fault, leveraging the benefits of multi-phase machines [56], since the winding could then be operated with 5 phases, instead of 2. Finally, the need of a position sensor has proved as a drawback for reliability. Therefore, the performance of the machine with the employment of an angle estimator, such as in [57], should be evaluated.

To improve the capabilities of this motor, the most obvious approach is to have a neutral connection to the inverter on standby, along with active switching. This configuration, as mentioned in chapter 3, can output close to nominal torque with minimal hardware expenses. If wire ratings are increased, this configuration can provide rated torque.

A more expensive but robust configuration is to have a phase leg on standby, ready to replace the faulty leg itself. This method does not require resizing of the conductors, or a change in control algorithm, but is more expensive due to the SCR needed to isolate the faulty phase and connect the redundant one.

Bibliography

[1] M. Ruba and L. Szabo. “Fault Tolerant Electrical Machines. State of the Art and Future Directions”. In: *Journal of Computer Science and Control Systems* (2008).

[2] E. A. Bhuiyan et al. “A survey on Fault Diagnosis and Fault Tolerant Methodologies for Permanent Magnet Synchronous Machines”. In: *Inernational Journal of Automation and Computing* 17 (2020), pp. 763–787. DOI: `https://doi.org/10.1007/s11633-020-1250-3`.

[3] B. A. Welchko et al. “Fault Tolerant Three-Phase AC Motor Drive Topologies: A Comparison of Features, Cost, and Limitations”. In: *IEEE Transactions on Power Electronics* 19.4 (2004), pp. 1108–1116. DOI: `10.1109/TPEL.2004.830074`.

[4] Christian Du-Bar. “Design and analysis of a fault-tolerant fractional slot PMSM for a vehicle application”. In: (2016). DOI: `ISBN978-91-7597-467-5`.

[5] Stephen Umans. *Electric machinery.* McGraw-Hill, 2002. ISBN: 9780070530393.

[6] J. Åström and T. Thiringer. “Time efficient FEM modeling of a PMSM by iteration between field calculations and state”. In: (2016), pp. 2112–2118. DOI: `10.1109/ICELMACH.2016.7732814`.

[7] Prabha Kundur. *Power System Stability and Control.* McGraw-Hill, Inc., 1994. Chap. 3.1.

[8] Oskar Wallmark. “Control of Permanent-Magnet Synchronous Machines in Automotive Applications”. In: (2006). DOI: `ISBN91-7291-846-2`.

[9] R. Islam and A Fardoun. “Permanent-Magnet Synchronous Motor Magnet Designs With Skewing for Torque Ripple and Cogging Torque Reduction”. In: *IEEE Transactions on Industry Applications* 45.1 (2009). DOI: `10.1109/TIA.2008.2009653`.

[10] M. Kozovsky and P. Blaha. “Double three-phase PMSM structures for fail operational control”. In: (2019).

[11] O. A. Mohammed, S. Liu, and Z. Liu. “Physical modeling of PM synchronous motors for integrated coupling with Machine drives”. In: *IEEE Transactions on Magnetics* 41.5 (2005), pp. 1628–1631. DOI: `10.1109/TMAG.2005.846122`.

[12] O. A. Mohammed, S. Liu, and Z. Liu. “A Phase Variable PM Machine Model for Integrated Motor Drive Systems”. In: *2004 35rk Annual IEEE Power Elecrronics Specialisrs Conference* (2004).

[13] Muhammad H. Rashid. *Power Electronics Handbook*. Elsevier, 2007. ISBN: 0-12-088479-8.

[14] L. Harnefors. *Control of Variable-speed Drives*. Applied Signal Processing and Control, Department of Electronics, Mälardalen University, 2002. URL: `https://books.google.se/books?id=wyXXjwEACAAJ`.

[15] Colm J. O'Rourke et al. "A Geometric Interpretation of Reference Frames and Transformations: dq0, Clarke, and Park". In: *IEEE Transactions on Energy Conversion* 34.4 (2019), pp. 2070–2083. DOI: `10.1109/TEC.2019.2941175`.

[16] Myung Joon Nam et al. "Torque ripple reduction of an interior PM synchronous motor for electronic power steering". In: *2015 9th International Conference on Power Electronics and ECCE Asia (ICPE-ECCE Asia)*. 2015, pp. 2445–2450. DOI: `10.1109/ICPE.2015.7168115`.

[17] Zhenbao Pan et al. "Combined Resonant Controller and Two-Degree-of-Freedom PID Controller for PMSLM Current Harmonics Suppression". In: *IEEE Transactions on Industrial Electronics* 65.9 (2018), pp. 7558–7568. DOI: `10.1109/TIE.2018.2793232`.

[18] Suk-Hee Lee et al. "A novel control method for reducing torque ripple in PMSM applied for Electric Power Steering". In: *2008 International Conference on Electrical Machines and Systems*. 2008, pp. 3142–3145.

[19] Heonyoung Kim and Subhashish Bhattacharya. "A Novel Current Control Strategy Based on Harmonic Voltage Injection for Power Losses Reduction of PMSMs with Non-Sinusoidal Back-EMF". In: *2019 IEEE Industry Applications Society Annual Meeting*. 2019, pp. 1–6. DOI: `10.1109/IAS.2019.8912372`.

[20] Xiaoyuan Wang. "Analysis of Harmonic Current in Permanent Magnet Synchronous Motor and Its Effect on Motor Torque". In: *Journal of Electromagnetic Analysis and Application* 4 (Jan. 2012), pp. 15–20. DOI: `10.4236/jemaa.2012.41003`.

[21] Zhuohang Li et al. "Single- and Two-Phase Open-Circuit Fault Tolerant Control for Dual Three-Phase PM Motor Without Phase Shifting". In: *IEEE Access* 8 (2020), pp. 171945–171955. DOI: `10.1109/ACCESS.2020.3024736`.

[22] Chandana Jayampathi Gajanayake et al. "Fault tolerant control method to improve the torque and speed response in PMSM drive with winding faults". In: *2011 IEEE Ninth International Conference on Power Electronics and Drive Systems*. 2011, pp. 956–961. DOI: `10.1109/PEDS.2011.6147371`.

[23] Yuliang Guo et al. "An Adaptive Torque Ripple Suppression Method of Three-Phase PMSM During Single-Phase Open-Circuit Fault-Tolerant Operation". In: *2019 22nd International Conference on Electrical Machines and Systems (ICEMS)*. 2019, pp. 1–5. DOI: `10.1109/ICEMS.2019.8921740`.

[24] Gaolin Wang, Guoqiang Zhang, and Dianguo Xu. *Position Sensorless Control Techniques for Permanent Magnet Synchronous Machine Drives*. Springer, 2020. DOI: `https://doi.org/10.1007/978-981-15-0050-3`.

[25] J. A. Haylock et al. “Operation of a fault tolerant PM drive for an aerospace fuel pump application”. In: (1997), pp. 133–137. DOI: `10.1049/cp:19971053`.

[26] M. O. E. Aboelhassan et al. “A fault-tolerant control scheme for a dual flux-switching permanent magnet motor drive”. In: (2011), pp. 1–6. DOI: `10.1109/ICEMS.2011.6073481`.

[27] B.A. Welchko et al. “IPM synchronous machine drive response to symmetrical and asymmetrical short circuit faults”. In: *IEEE Transactions on Energy Conversion* 18.2 (2003), pp. 291–298. DOI: `10.1109/TEC.2003.811746`.

[28] S. Bolognani, M. Zordan, and M. Zigliotto. “Experimental fault-tolerant control of a PMSM drive”. In: *IEEE Transactions on Industrial Electronics* 47.5 (2000), pp. 1134–1141. DOI: `10.1109/41.873223`.

[29] Joachim Härsjö. “Modeling and Analysis of PMSM with Turn-To-Turn Fault”. In: (2016).

[30] N. Bianchi, M. Dai Pré, and S. Bolognani. “Design of a Fault-Tolerant IPM Motor for Electric Power Steering”. In: *IEEE TRANSACTIONS ON VEHICULAR TECHNOLOGY* 55.4 (2006), pp. 1102–1111. DOI: `10.1109/TVT.2006.877716`.

[31] et al. A. Kontarcek. “Operation of a PMSM after Single Open-Phase Fault”. In: *International Conference-Workshop Compatibility And Power Electronics* (2013), pp. 177–181. DOI: `10.1109/CPE.2013.6601150`.

[32] Amr Saleh, Ghada Ahmed Abdel Nada Sayed, and Mona Nagieb Eskander. “Fault-Tolerant Control of Permanent Magnet Synchronous Motor Drive under Open-Phase Fault”. In: *Advances in Science, Technology and Engineering Systems Journal* 6.5 (2020), pp. 455–463. DOI: `10.25046/aj050654`.

[33] N. Bianchi et al. “Innovative remedial strategies for inverter faults in IPM synchronous motor drives”. In: *IEEE Transactions on Energy Conversion* 18.2 (2003), pp. 306–314. DOI: `10.1109/TEC.2002.808334`.

[34] P. Giangrande et al. “Braking Torque Compensation Strategy and Thermal Behavior of a Dual Three-Phase Winding PMSM During Short-Circuit Fault”. In: *2019 IEEE International Electric Machines Drives Conference (IEMDC)*. 2019, pp. 2245–2250. DOI: `10.1109/IEMDC.2019.8785164`.

[35] Arun Gandhi, Timothy Corrigan, and Leila Parsa. “Recent Advances in Modeling and Online Detection of Stator Interturn Faults in Electrical Motors”. In: *IEEE Transactions on Industrial Electronics* 58.5 (2011), pp. 1564–1575. DOI: `10.1109/TIE.2010.2089937`.

[36] Xinxiu Zhou et al. “PMSM Open-Phase Fault-Tolerant Control Strategy Based on Four-Leg Inverter”. In: *IEEE Transactions on Power Electronics* 35.3 (2020), pp. 2799–2808. DOI: `10.1109/TPEL.2019.2925823`.

[37] Giuseppe Scarcella et al. “Fault-Tolerant Capability of Deadbeat-Direct Torque and Flux Control for Three-Phase PMSM Drives”. In: *IEEE Transactions on Industry Applications* 53.6 (2017), pp. 5496–5508. DOI: `10.1109/TIA.2017.2743070`.

[38] Mongi Moujahed et al. “Fault detection and fault-tolerant control of power converter fed PMSM”. In: *Electrical Engineering* 98.1 (201), pp. 121–131. DOI: `10.1007/s00202-015-0350-5`.

[39] R.L. de Araujo Ribeiro et al. “Fault-tolerant voltage-fed PWM inverter AC motor drive systems”. In: *IEEE Transactions on Industrial Electronics* 51.2 (2004), pp. 439–446. DOI: `10.1109/TIE.2004.825284`.

[40] Xuefeng Jiang et al. “Short-Circuit Fault-Tolerant Operation of Dual-Winding Permanent-Magnet Motor Under the Four-Quadrant Condition”. In: *IEEE Transactions on Industrial Electronics* 66.9 (2019), pp. 6789–6798. DOI: `10.1109/TIE.2018.2878131`.

[41] Guodong Feng et al. “Open-Phase Fault Modeling and Optimized Fault-Tolerant Control of Dual Three-Phase Permanent Magnet Synchronous Machines”. In: *IEEE Transactions on Power Electronics* 34.11 (2019), pp. 11116–11127. DOI: `10.1109/TPEL.2019.2900599`.

[42] Y. Zhao and T.A. Lipo. “Space vector PWM control of dual three phase induction machine using vector space decomposition”. In: *Proceedings of 1994 IEEE Industry Applications Society Annual Meeting*. Vol. 1. 1994, 742–749 vol.1. DOI: `10.1109/IAS.1994.345429`.

[43] Xiaolin KUANG et al. “Research on a six-phase permanent magnet synchronous motor system at dual-redundant and fault tolerant modes in aviation application”. In: *Chinese Journal of Aeronautics* 30.4 (2017), pp. 1548–1560. ISSN: 1000-9361. DOI: `https://doi.org/10.1016/j.cja.2017.05.001`. URL: `https://www.sciencedirect.com/science/article/pii/S1000936117301048`.

[44] B.A. Welchko et al. “Fault tolerant three-phase AC motor drive topologies; a comparison of features, cost, and limitations”. In: *IEEE International Electric Machines and Drives Conference, 2003. IEMDC’03.* Vol. 1. 2003, 539–546 vol.1. DOI: `10.1109/IEMDC.2003.1211315`.

[45] Yonghui Liao. “Analysis of fault conditions in permanent magnet in-wheel motors”. In: *Master Thesis KTH* (2011). DOI: `diva2:470634`. URL: `http://kth.diva-portal.org/smash/record.jsf?pid=diva2%5C%3A470634&dswid=9967`.

[46] Ge Qi, Zhen Wang, and Bing-ying Zhao. “Sliding mode control strategy for dual three-phase 180° electrical degrees permanent magnet synchronous motor”. In: *2017 IEEE 2nd Information Technology, Networking, Electronic and Automation Control Conference (ITNEC)*. 2017, pp. 818–822. DOI: `10.1109/ITNEC.2017.8284848`.

[47] Yashan Hu, Z. Q. Zhu, and Milijana Odavic. “Comparison of Two-Individual Current Control and Vector Space Decomposition Control for Dual Three-Phase PMSM”. In: *IEEE Transactions on Industry Applications* 53.5 (2017), pp. 4483–4492. DOI: `10.1109/TIA.2017.2703682`.

[48] Pengcheng Liu et al. "Remedial Strategies of Cascaded CSIs-fed Dual Three-phase PMSM Drives under One-phase Open-circuit Faults". In: *2019 IEEE Energy Conversion Congress and Exposition (ECCE).* 2019, pp. 6134–6139. DOI: `10.1109/ECCE.2019.8912699`.

[49] Jiayuan Zhang, Wei Zhan, and Mehrdad Ehsani. "Fault-Tolerant Control of PMSM With Inter-Turn Short-Circuit Fault". In: *IEEE Transactions on Energy Conversion* 34.4 (2019), pp. 2267–2275. DOI: `10.1109/TEC.2019.2936225`.

[50] Andraž Kontarček et al. "Cost-Effective Three-Phase PMSM Drive Tolerant to Open-Phase Fault". In: *IEEE Transactions on Industrial Electronics* 62.11 (2015), pp. 6708–6718. DOI: `10.1109/TIE.2015.2437357`.

[51] Andraž Kontarček et al. "Single Open-phase Fault Detection with Fault-Tolerant Control of an Inverter-fed Permanent Magnet Synchronous Machine". In: *Automatika* 55.4 (2014), pp. 474–486. DOI: `10.7305/automatika.2014.12.624`. eprint: `https://doi.org/10.7305/automatika.2014.12.624`. URL: `https://doi.org/10.7305/automatika.2014.12.624`.

[52] M. Liserre R. Teodorescu F. Blaabjerg and P.C. Loh. "Proportional-resonant controllers and filters for grid-connected voltage-source converters". In: *IEE Proceedings* 153.5 (2006), pp. 750–762. DOI: `10.1049/ip-epa:20060008`. URL: `https://digital-library.theiet.org/content/journals/10.1049/ip-epa_20060008`.

[53] Charles Lorenzini et al. "A model-free tuning method for proportional-multi-resonant controllers". In: *arXiv e-prints*, arXiv:2007.01942 (July 2020), arXiv:2007.01942. arXiv: `2007.01942 [eess.SY]`.

[54] Samuli Kallio et al. "Decoupled d-q Model of Double-Star Interior-Permanent-Magnet Synchronous Machines". In: *IEEE Transactions on Industrial Electronics* 60.6 (2013), pp. 2486–2494. DOI: `10.1109/TIE.2012.2216241`.

[55] Jussi Karttunen et al. "Decoupled Vector Control Scheme for Dual Three-Phase Permanent Magnet Synchronous Machines". In: *IEEE Transactions on Industrial Electronics* 61.5 (2014), pp. 2185–2196. DOI: `10.1109/TIE.2013.2270219`.

[56] Mario J. Duran, Emil Levi, and Federico Barrero. "Multiphase Electric Drives: Introduction". In: *Wiley Encyclopedia of Electrical and Electronics Engineering.* American Cancer Society, pp. 1–26. ISBN: 9780471346081. DOI: `https://doi.org/10.1002/047134608X.W8364`.

[57] Oskar Wallmark, Lennart Harnefors, and Ola Carlson. "Control Algorithms for a Fault-Tolerant PMSM Drive". In: *IEEE Transactions on Industrial Electronics* 54.4 (2007), pp. 1973–1980. DOI: `10.1109/TIE.2007.895076`.

A

Appendix 1

Appendix 1 concerns the derivations and implementation of the dual-winding simulation model.

A.1 Current equation

Expanded current state equation derived in section 5.1 and 5.1.1. Showing the expression for current of phase a in winding 1. Where subscript 1 and 2 indicate winding set one and two and double digit subscripts denotes the element in the inductance matrix. Single letter subscripts a, b and c denotes phase quantities and subscript ab and bc line-to-line quantities.

$$\frac{d}{dt}i_{a_1} =$$

$$\begin{array}{l}
\mathrm{L}_{44}^{-1}(V_{ab_1} - R_{a_1}i_{a_1} + R_{b_1}i_{b_1} - \omega_r(\tfrac{d}{d\theta}L_{11}i_{a_1} + \tfrac{d}{d\theta}L_{12}i_{b_1} + \tfrac{d}{d\theta}L_{13}i_{a_2} + \tfrac{d}{d\theta}L_{14}i_{b_2}) - \\
\omega_r\tfrac{d}{d\theta}(\psi_{ma_1} - \psi_{mb_1})) + \\
\mathrm{L}_{34}^{-1}(V_{bc_1} - R_{c_1}i_{a_1} - (R_{b_1} + R_{c_1})i_{b_1} - \omega_r(\tfrac{d}{d\theta}L_{21}i_{a_1} + \tfrac{d}{d\theta}L_{22}i_{b_1} + \tfrac{d}{d\theta}L_{23}i_{a_2} + \tfrac{d}{d\theta}L_{24}i_{b_2}) - \\
\omega_r\tfrac{d}{d\theta}(\psi_{mb_1} - \psi_{mc_1})) + \\
\mathrm{L}_{24}^{-1}(V_{ab_2} - R_{a_2}i_{a_2} + R_{b_2}i_{b_2} - \omega_r(\tfrac{d}{d\theta}L_{31}i_{a_1} + \tfrac{d}{d\theta}L_{32}i_{b_1} + \tfrac{d}{d\theta}L_{33}i_{a_2} + \tfrac{d}{d\theta}L_{44}i_{b_2}) - \\
\omega_r\tfrac{d}{d\theta}(\psi_{ma_2} - \psi_{mb_2})) - \\
\mathrm{L}_{14}^{-1}(V_{bc_2} - R_{c_2}i_{a_2} - (R_{b_2} + R_{c_2})i_{b_2} - \omega_r(\tfrac{d}{d\theta}L_{41}i_{a_1} + \tfrac{d}{d\theta}L_{42}i_{b_1} + \tfrac{d}{d\theta}L_{43}i_{a_2} + \tfrac{d}{d\theta}L_{44}i_{b_2}) - \\
\omega_r\tfrac{d}{d\theta}(\psi_{mb_2} - \psi_{mc_2}))\text{(A.1)}
\end{array}$$

Line to line inductance matrix of the healthy dual winding machine is expressed as

$$\mathbb{L} = \begin{bmatrix}
(L_{a1a1} - L_{a1c1} - L_{b1a1} + L_{b1c1}) & (L_{a1b1} - L_{a1c1} - L_{b1b1} + L_{b1c1}) & (L_{a1a2} - L_{a2b1} - L_{a1c2} + L_{b1c2}) & (L_{a1b2} - L_{a1c2} - L_{b1b2} + L_{b1c2}) \\
(L_{a1b1} - L_{b1c1} - L_{c1a1} + L_{c1c1}) & (L_{b1b1} - L_{b1c1} - L_{c1b1} + L_{c1c1}) & (L_{a2b1} - L_{a2c1} - L_{b1c2} + L_{c1c2}) & (L_{b1b2} - L_{b2c1} - L_{b1c2} + L_{c1c2}) \\
(L_{a1a2} - L_{a1b2} - L_{a2c1} + L_{b2c1}) & (L_{a2b1} - L_{b1b2} - L_{a2c1} + L_{b2c1}) & (L_{a2a2} - L_{a2b2} - L_{a2c2} + L_{b2c2}) & (L_{a2b2} - L_{b2b2} - L_{a2c2} + L_{b2c2}) \\
(L_{a1b2} - L_{b2c1} - L_{c2a1} + L_{c1c2}) & (L_{b1b2} - L_{b2c1} - L_{c2b1} + L_{c1c2}) & (L_{a2b2} - L_{a2c2} - L_{b2c2} + L_{c2c2}) & (L_{b2b2} - L_{b2c2} - L_{b2c2} + L_{c2c2})
\end{bmatrix} \tag{A.2}$$

where 1 and 2 in the subscripts denotes the two windings and a,b and c the respective phases.

A.2 Dual winding Simulink model

Implementation of the electrical equations for the dual winding machine as discussed in section 5.1.3.

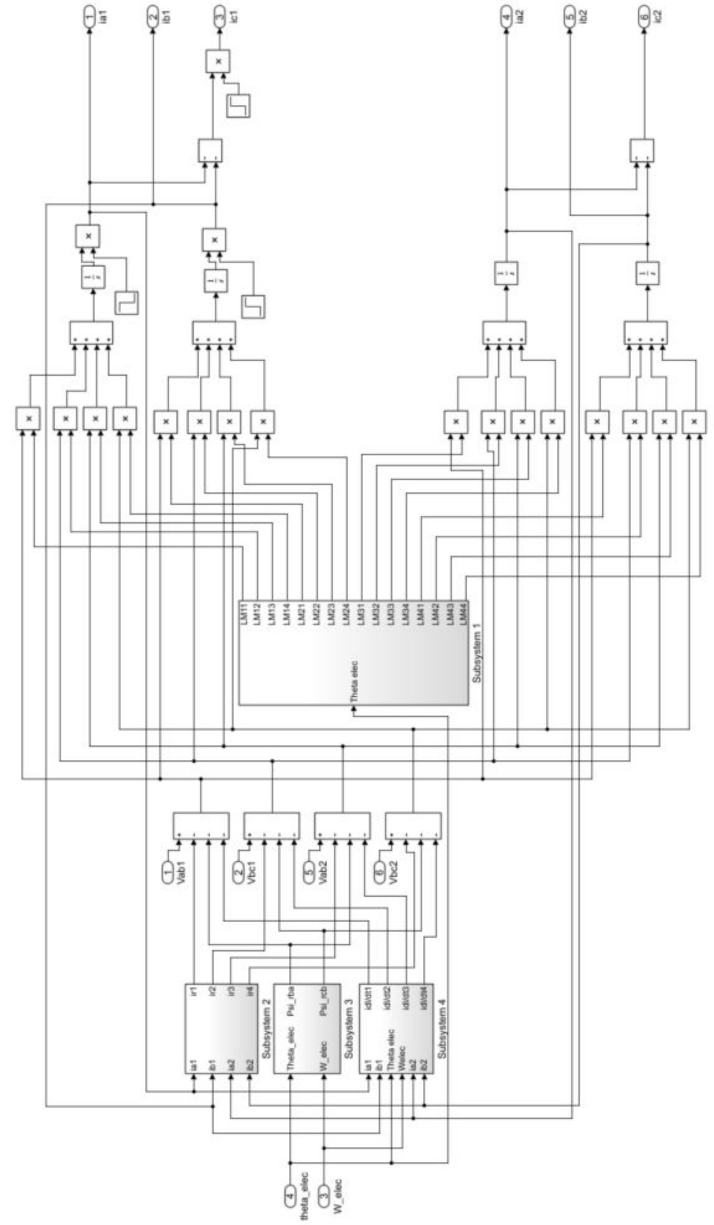
1 ia1
2 ib1
3 ic1
4 ia2
5 ib2
6 ic2
LM11
LM12
LM13
LM14
LM21
LM22
LM23
LM24
LM31
LM32
LM33
LM34
LM41
LM42
LM43
LM44
Theta elec
Subsystem 1
1 Vab1
2 Vbc1
5 Vab2
6 Vbc2
ir1
ir2
ir3
ir4
ia1
ib1
ia2
ib2
Subsystem 2
Psi_rfa
Psi_rcb
Theta_elec
W_elec
Subsystem 3
idi/dt1
idi/dt2
idi/dt3
idi/dt4
ia1
ib1
Theta elec
Welec
ia2
ib2
Subsystem 4
4 theta_elec
3 W_elec

Figure A.1: Line-to-line dual winding electrical machine model

B

Appendix 2

B.1 Resonant controller derivation

Derivation of (5.12) for Simulink implementation as described in section 5.3.3.

$$G_c = \frac{out}{in} = \frac{K_r s}{s^2 + 2\omega_c s + (n\omega_e)^2} \tag{B.1}$$

$$out(s^2 + 2\omega_c s + (n\omega_e)^2) = inK_r s \tag{B.2}$$

$$\frac{out}{K_r s}(s^2 + 2\omega_c s + (n\omega_e)^2) = in \tag{B.3}$$

$$\frac{out}{K_r}s + \frac{out}{K_r}2\omega_c + \frac{out}{K_r s}(n\omega_e)^2 = in \tag{B.4}$$

$$\frac{out}{K_r}s = in - \frac{out}{K_r}2\omega_c - \frac{out}{K_r s}(n\omega_e)^2 \tag{B.5}$$

$$out = \frac{K_r}{s}(in - \frac{out}{K_r}2\omega_c - \frac{out}{K_r s}(n\omega_e)^2) \tag{B.6}$$

DEPARTMENT OF ELECTRICAL ENGINEERING
CHALMERS UNIVERSITY OF TECHNOLOGY
Gothenburg, Sweden
www.chalmers.se